









# Prompt fission neutron yields in thermal fission of $^{235}\text{U}$ and spontaneous fission of $^{252}\text{Cf}$

A. Al-Adili <sup>\*</sup>, D. Tarrío , K. Jansson, V. Rakopoulos , A. Solders , and S. Pomp   
*Department of Physics and Astronomy, Uppsala University, Box 516, 751 20 Uppsala, Sweden*

A. Göök <sup>†</sup>, F.-J. Hamsch, S. Oberstedt, and M. Vidali   
*European Commission, DG Joint Research Centre, Directorate G - Nuclear Safety and Security, Unit G.2 SN3S, 2440 Geel, Belgium*

 (Received 5 June 2020; revised 7 September 2020; accepted 9 October 2020; published 10 December 2020)

**Background:** The sharing of excitation energy between the fission fragments is one of the key issues in studying nuclear fission. One way to address this is by studying prompt-fission neutron multiplicities as a function of other fission observables such as the mass,  $\bar{\nu}(A)$ . These are vital benchmark data for both fission and nuclear deexcitation models, putting constraints on the fragment excitation energy and hence on the competing prompt neutron/ $\gamma$ -ray emission. Despite numerous detailed studies, recent measurements done at JRC-Geel with the SCINTIA array in the epithermal region show surprisingly strong discrepancies to earlier thermal fission data and the Wahl systematics.

**Purpose:** The purpose was to perform measurements of the prompt-fission neutron multiplicity, as a function of fragment mass and total kinetic energy (TKE), in  $^{235}\text{U}(\text{n}_{\text{th}}, \text{f})$  and  $^{252}\text{Cf}(\text{sf})$ , to verify and extend the SCINTIA results. Another goal was to validate the analysis methods, and prepare for planned investigations at excitation energies up to 5.5 MeV.

**Methods:** The experiments were conducted at the former 7 MV Van de Graaff facility in JRC-Geel, using a Twin Frisch-Grid Ionization Chamber and two liquid scintillation detectors. A neutron beam with an average energy of 0.5 MeV was produced via the  $^7\text{Li}(\text{p}, \text{n})$  reaction. The neutrons were thermalized by a 12 cm thick block of paraffin. Digital data acquisition systems were utilized. Comprehensive simulations were performed to verify the methodology and to investigate the role of the mass and energy resolution on measured  $\bar{\nu}(A)$  and  $\bar{\nu}(\text{TKE})$  values. The simulation results also revealed that the  $\partial\bar{\nu}(A)/\partial A$  and  $\partial\overline{\text{TKE}}/\partial\bar{\nu}$  are affected by the mass and energy resolution. However, the effect is small for the estimated resolutions of this work. Detailed Fluka simulations were performed to calculate the fraction of thermal neutron-induced fission, which was estimated to be about 98%.

**Results:** The experimental results on  $\bar{\nu}(A)$  are in good agreement with earlier data for  $^{252}\text{Cf}(\text{sf})$ . For  $^{235}\text{U}(\text{n}_{\text{th}}, \text{f})$ , the  $\bar{\nu}(A)$  data is very similar to the data obtained with SCINTIA, and therefore we verify these disclosed discrepancies to earlier thermal data and to the Wahl evaluation. The experimental results on  $\bar{\nu}(\text{TKE})$  are also in agreement with the data at epithermal energies. For  $^{252}\text{Cf}(\text{sf})$  a slope value of  $\partial\overline{\text{TKE}}/\partial\bar{\nu} = (-12.9 \pm 0.2)$  MeV/n was obtained. For  $^{235}\text{U}(\text{n}_{\text{th}}, \text{f})$  the value is  $(-12.0 \pm 0.1)$  MeV/n. Finally, the neutron spectrum in the center-of-mass system was derived and plotted as a function of fragment mass.

**Conclusions:** This work clearly proves the lack of accurate correlation between fission fragment and neutron data even in the best-studied reactions. The new results highlight the need of a new evaluation of the prompt-fission multiplicity for  $^{235}\text{U}(\text{n}_{\text{th}}, \text{f})$ .

DOI: [10.1103/PhysRevC.102.064610](https://doi.org/10.1103/PhysRevC.102.064610)

## I. INTRODUCTION

Prompt neutrons carry crucial signature information on the scission configuration in nuclear fission. Already in 1954,

<sup>\*</sup>ali.al-adili@physics.uu.se

<sup>†</sup>Present address: KTH Royal Institute of Technology, 10691 Stockholm, Sweden.

*Published by the American Physical Society under the terms of the [Creative Commons Attribution 4.0 International](https://creativecommons.org/licenses/by/4.0/) license. Further distribution of this work must maintain attribution to the author(s) and the published article's title, journal citation, and DOI. Funded by [Bibsam](https://www.bibsam.com/).*

Fraser and Milton discovered a correlation between the neutron yields and the fragment mass distribution [1]. Early fission theory was based on the liquid drop model and could not account for nuclear shell effects and, therefore, not for the asymmetric fragment mass split and the strong mass dependence in the prompt-fission neutron yield [2]. A substantial impact of nuclear shell effects is observed in various fission observables, e.g., mass yields, neutron and  $\gamma$ -ray yields, and isomeric fission [3]. In many cases, the dependence of a fission observable on the excitation energy of the compound nucleus is not well known. This is the case for the fragment-specific neutron multiplicity  $\bar{\nu}(A)$ . To understand the sharing of total excitation energy (TXE) in the fission process and the impact of shell effects, it is important to study how such

effects may wash out with increasing incident neutron energy. Experimental data are, however, scarce, particularly in the case of fission neutrons [4]. Therefore, systematic investigations are needed for various fissioning systems.

In this study we present two experiments, one for  $^{252}\text{Cf}(\text{sf})$  and the second for  $^{235}\text{U}(\text{n}_{\text{th}}, \text{f})$ . We focus on the average fission neutron multiplicity as a function of fragment mass and the total kinetic energy (TKE). The measurement of  $^{252}\text{Cf}(\text{sf})$  served as a proof of principle and a calibration case, since it is a widely studied fissioning system. On the other hand, the experiment on  $^{235}\text{U}(\text{n}_{\text{th}}, \text{f})$  aims at serving as a reference for an upcoming  $\bar{\nu}(A)$  measurement at higher excitation energies. The measured thermal fission of  $^{235}\text{U}$  data also complements the recent investigations at JRC-Geel with the SCINTIA neutron array [5]. The latter was employed to measure the  $^{235}\text{U}(\text{n}, \text{f})$  reaction in the epithermal range [0.26 eV, 45 keV] and revealed surprising differences to earlier thermal fission neutron data and evaluations [6–9]. The discrepancies could be owed to superior experimental mass and energy resolutions, refined data analysis and use of digital acquisition systems. It could also be partly caused by the presence of strong resonances in the studied energy region. Therefore, our data investigate these discrepancies and their cause. We utilized similar techniques and digital acquisition system as in the case with SCINTIA, but employed different detectors, fissile targets and accelerator-based neutron source, and most importantly, measured in a thermal neutron spectrum.

In parallel to the experimental study, we performed detailed simulations to verify the methodology and to evaluate how the stringent kinematic cuts (also applied in Refs. [10,11]) affect the  $\bar{\nu}(A)$  and  $\bar{\nu}(\text{TKE})$  derivation, and to explore the role of the mass resolution on the deduced data.

## II. EXPERIMENTAL SETUP AND PRINCIPLE

The experiments were performed at the former Van de Graaff accelerator of the Joint Research Centre in Geel, Belgium. The setup used for this work is depicted in Fig. 1(a) and is composed of a Twin Frisch-Grid Ionization Chamber (TFGIC) for fission fragment (FF) detection and two EJ-301 liquid scintillation detectors (NE-213 equivalent) serving as neutron detectors (NDR and NDL). In between the chamber and the neutron source, a 12 cm thick paraffin block was used to thermalize the beam. The neutron detectors were placed along the chamber symmetry axis facing the fission target, perpendicular to the direction of the proton beam. The cylinder symmetric geometry allows extracting the direction of motion of the fission fragments relative to neutron emission. Both fragments are detected back to back and the mass distribution is calculated from the measured kinetic energies, by evoking momentum and total mass conservation [12]. By calculating the mass yields, with and without coincidence requirement between the TFGIC and the liquid scintillation detectors, the neutron emission probability can be obtained (independently for the two NDs), as a function of the pre-neutron emission mass ( $A_{\text{pre}}$ ). The ratio of the coincidence to noncoincidence distributions permits us to determine both  $\bar{\nu}(A)$  and  $\bar{\nu}(\text{TKE})$ .

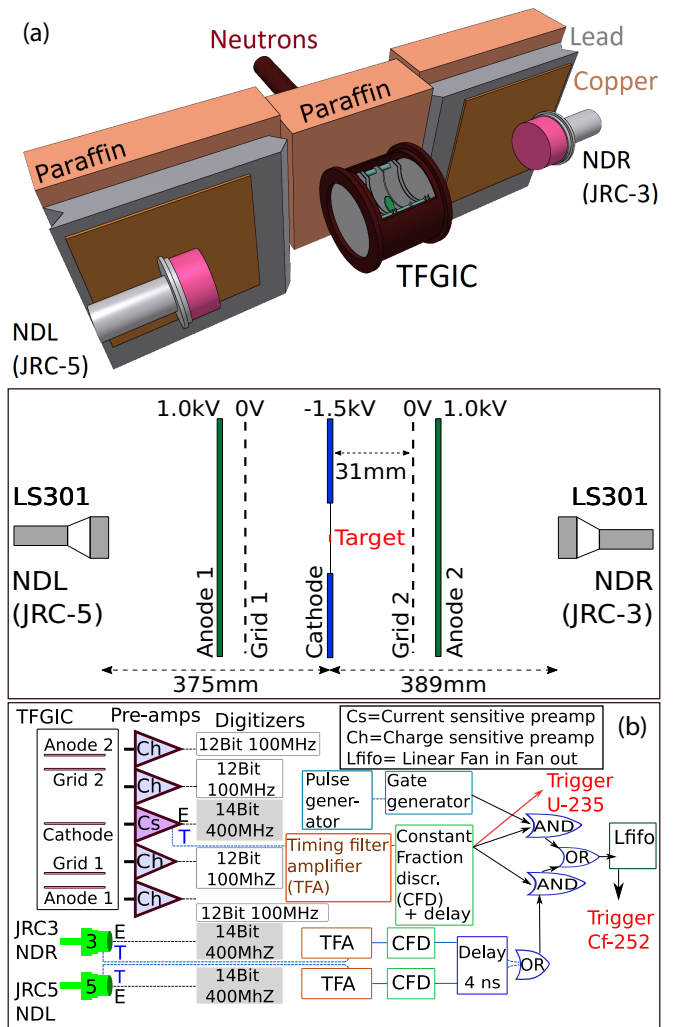


FIG. 1. (a) A schematic view of the experimental setup, with two EJ-301 liquid scintillation neutron detectors, left (NDL, ID JRC-5) and right (NDR, ID JRC-3), and the Twin Frisch-Grid Ionization Chamber (TFGIC). The fission target was placed in the center of the cathode electrode. (b) The electronics and digital acquisition system used in the experiment. Two different trigger schemes were used for the two measurements (see text for details).

### A. Data acquisition and trigger

Digital data acquisition systems were utilized to record every signal from the chamber and the neutron detectors [see Fig. 1(b)] [13]. Since the cathode and the two NDs signals were used to extract timing information, a 400 MHz sampling frequency was needed, whereas for the anodes and grids, sampling rates of 100 MHz were sufficient. The acquisition system was triggered slightly different in the two cases, due to a high spontaneous fission rate in  $^{252}\text{Cf}$ . In the case of  $^{252}\text{Cf}$ , the system was triggered by the coincidence condition between either of the two neutron detectors and the ionization chamber. Fission pulses, without coincidence requirement were also recorded continuously, however, due to the high fission rate, the noncoincident acquisition was scaled down by a factor 400. In the case of  $^{235}\text{U}$ , the trigger was obtained

from the chamber solely, and the coincidence condition was invoked in the off-line analysis.

### B. Thermal neutron beam production

For the purpose of measuring  $^{235}\text{U}(n_{\text{th}}, f)$ , a 0.5 MeV neutron beam was produced via the  $^7\text{Li}(p, n)$  reaction, and thermalized by a block of paraffin with a thickness of 12 centimeter, placed in front of the chamber [see Fig. 1(a)]. A proton beam with an energy  $E_p \approx 2.3$  MeV was used to irradiate a LiF target ( $1.582 \text{ mg/cm}^2$ ) to produce a neutron beam between 0.3 and 0.6 MeV (average of 0.5 MeV). The average proton beam current during the experimental campaign was fluctuating around  $5 \mu\text{A}$ . The neutron beam energy was chosen to be below the detection threshold of the neutron detector that is around 0.7 MeV. Thus, we avoid misidentifying beam neutrons as fission neutrons. Comprehensive simulations were performed to simulate the neutron moderation in the paraffin block and to calculate the neutron flux at the target position. The vast majority of all fission events in the case of  $^{235}\text{U}(n, f)$  were caused by thermal neutrons (see Sec. III A).

The liquid scintillation detectors (SCIONIX EJ-301,  $\phi = 10$  cm,  $h = 5$  cm,  $\text{HV} = 1.1$  kV) were characterized by Kormilov *et al.* [17]. The distances between the center of the active region of the detectors and the fission source were 389 mm for NDR (ID JRC-3) and 375 mm for ND (ID JRC-5). ND is the detector facing the sample side of the target, see Fig. 1(a). The geometrical coverage was about 0.5% for each detector. The ionization chamber was operated with P-10 gas, at a pressure of 107 kPa and a flow rate of about 0.1 l/min. Anode and cathode plates were supplied with high voltage, 1.0 kV and  $-1.5$  kV, respectively, whereas the grids were grounded. The Cf sample (different from the sample used in Ref. [11]) was deposited on a Ni backing (250 nm) via electrodeposition and had a strength of about 5000 f/sec at the time of the experiment. The uranium sample was produced via vacuum evaporation and has an active diameter of  $(30.11 \pm 0.02)$  mm and an areal density of  $(117.1 \pm 0.7) \mu\text{g/cm}^2$ . It was deposited on a polyimide backing ( $35 \mu\text{g/cm}^2$ ) and had an isotopic purity of 99.9336(14)%. The neutron detectors were shielded from the beam (both from neutrons and  $\gamma$  rays) by a wall of paraffin (10 cm), lead (5 cm), and Cu (5 mm).

## III. SIMULATIONS

### A. Neutron moderation and fission rates

FLUKA simulations (version 2011.2x.8 [14,15], assisted by the Flair interface 2.3-0 [16]) were performed to calculate the neutron thermalization and to determine the neutron flux at the fissile target position. The implemented geometry in Flair can be seen in Fig. 1(a).

The neutron production was simulated using the NeuSDesc flux calculator [18], which takes the energy spectrum and angular distribution of the  $^7\text{Li}(p, n)$  reaction into account. The resulting neutron flux at the fissile target position is plotted (in isoenergic units) in Fig. 2 together with the fission cross section of  $^{235}\text{U}$ , taken from the ENDF-B-VIII.0 library. Figure 2 also indicates the epithermal energy region of the

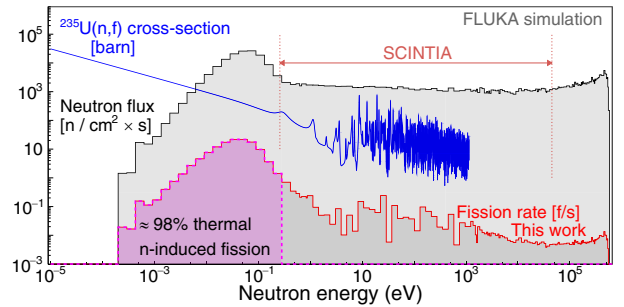


FIG. 2. FLUKA simulations [14–16] to model the neutron moderation in the  $^{235}\text{U}(n_{\text{th}}, f)$  experiment. The fission rate (red histogram) was calculated using the ENDF-B-VIII.0 cross section library (blue line) and the neutron flux (gray shaded histogram). The fraction of thermal neutron-induced events is around 98%, indicated by the integrated thermal peak in magenta [0 eV, 0.26 eV]. The flux and the fission rate are plotted in isoenergic units, and the different curves share the same numerical scale in the  $Y$  axis. The energy range measured with SCINTIA is also indicated by the arrow.

experimental data measured with SCINTIA. The fission rate was calculated assuming a beam current of  $5 \mu\text{A}$ , and was about 48 f/s. This result is compatible with the observed fission rate in the on-line acquisition, which was ranging between 40 and 50 Hz, measured for a beam current that oscillated around  $5 \mu\text{A}$ . What is most relevant is the fraction of fission events induced by thermal neutrons. This value was found by integrating the fission-rate histogram in the region corresponding to the thermal neutron peak [0 eV, 0.26 eV], as indicated by the magenta shaded area in Fig. 2. The calculated thermal-fission fraction was about 98%.

### B. Fission neutron detection

In order to validate the methodology, and to study the impact of mass and energy resolutions on the final determined neutron yields, we performed detailed simulations of the  $^{252}\text{Cf}(sf)$  reaction, using the GEF code as event generator [19]. The event-by-event output of GEF was treated to account for relativistic kinematics and for the effect of the neutron recoils to the fragments in each event (see Ref. [20] for details).

We assume that fission fragments evaporate fission neutrons after acquiring full velocity. Figure 3 illustrates a vector diagram of the neutron emission, where the fissile target is placed at  $(0,0,0)$  in  $(x, y, z)$  and  $(x', y', z')$  is the reference frame of the moving fragment. An isotropic neutron emission is normally assumed in the center-of-mass frame ( $\theta_{\text{c.m.}}$ ) of the emitting fragment [21,22]. We define the angle,  $\vartheta$ , to be between the symmetry axis of the chamber and the momentum vector of the emitted neutron ( $\vec{v}_L$ ). The neutron detector is positioned at  $\cos(\vartheta) = 1.0$ , and selects a narrow cone of detectable neutrons,  $\cos(\vartheta) \geq 0.99$ . Experimentally all detected neutrons are treated as emitted at  $\cos(\vartheta) = 1.0$ . The neutrons experience a kinematic boost, which makes the neutron angular distribution, in the laboratory frame ( $\theta_L$ ), strongly correlated with the fission axis ( $\vec{v}_f$ ). This is clearly observed in the correlation between  $\cos(\theta_f)$  and  $\cos(\vartheta)$ , as illustrated in Fig. 4(a). The principle of measuring  $\bar{\nu}(A)$  in this work

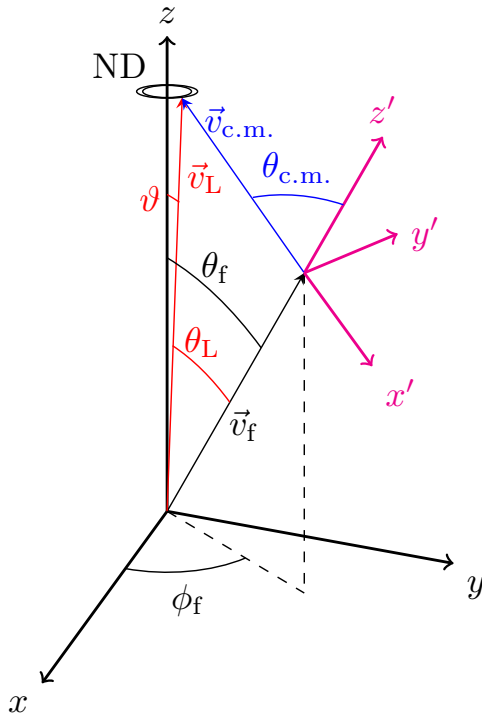


FIG. 3. A vector diagram of the neutron emission. The target is placed at (0,0,0) and the neutron detector is placed at (0,0,1). The vector  $\vec{v}_f$  is the fragment velocity, with  $\theta_f$  being the emission angle relative to the detector axis and  $\phi_f$  is the azimuthal angle.  $\vec{v}_{c.m.}$  is the neutron velocity in center-of-mass system of the emitting fragment (primed reference frame), and  $\vec{v}_L$  is the neutron laboratory velocity. The angles  $\theta_{c.m.,L}$  are the neutron angles in center-of-mass and laboratory systems. The angle between the neutron detector symmetry axis and the neutron laboratory momentum vector is  $\vartheta$ .

takes advantage of this kinematic boost, since the predominant amount of measured neutrons in each detector originates from fragments flying towards the same detector. The individual neutron  $\cos(\vartheta)$  distributions, emitted from fragments flying towards or away from the detector, are plotted in Fig. 4(b). The tiny gray highlighted area around  $\cos(\vartheta) = 1$  indicates the detectable neutrons. All center-of-mass emission angles contribute to these detected neutrons, albeit with some bias towards  $\cos(\theta_{c.m.}) = 1.0$ , due to a relatively high intrinsic detector threshold at  $E_n \approx 0.7$  MeV. The impact of this energy threshold is observed in Figs. 5(a) and 5(b), as a significant part of back-emitted neutrons is filtered out. The energy threshold alters the detected neutron spectrum, as it can be seen in the inset of Fig. 5(a), which leads to wrong neutron multiplicity results. To avoid this error, a selection in the neutron emission angle,  $\theta_{c.m.}$ , is necessary [5,10]. Figure 5(b) shows the neutron angle ( $\theta_{c.m.}$ ) versus the fragment angle ( $\theta_f$ ), for the neutrons reaching the detector, excluding laboratory energies below the intrinsic energy threshold. The  $\theta_{c.m.}$  cut is highlighted by the forward region in Fig. 5(b). This cut restores the neutron spectrum, as can be seen in the inset of Fig. 5(a). From the simulation we conclude that 99.7% of the neutrons selected in the forward region have laboratory energies above 0.7 MeV. This ensures that the detector neutron

threshold has a negligible impact. To perform the angular cut, we follow the vector diagram presented in Fig. 3, and transform from the laboratory to center-of-mass frame as follows [5,21]:

$$v_{c.m.}^2 = v_L^2 + v_f^2 - 2v_L v_f \cos(\theta_L)$$

$$\cos(\theta_{c.m.}) = (v_L \cos(\theta_L) - v_f)/v_{c.m.} \quad (1)$$

The kinematic cut is applied in the relative angle between neutrons and fragments, as only events with  $\cos(\theta_{c.m.}) \geq 0.0$  are taken into account. Therefore, only neutrons with laboratory velocities higher than the fragment velocity will be selected for further analysis:

$$\frac{v_f}{\cos(\theta_L)} \leq v_L. \quad (2)$$

The neutrons selected in the forward region, are thus used to determine  $\bar{v}(A)$  and  $\bar{v}(\text{TKE})$  from. As we will discuss later, one also needs to correct for the background of neutrons emitted backwards from the fragment flying away from the detector (highlighted in the backward region). The average neutron emission probability is determined by the ratio of coincidence and non-coincidence mass yield data. The simulated mass yields are plotted in Fig. 6(a), in coincidence with the neutron detector (blue shaded area and normalized yield in black) and without coincidence condition (red shaded area). Similarly, one can determine the average neutron emission probability, as a function of TKE, by considering the ratio of coincidence to noncoincidence TKE distributions [Fig. 6(b)]. Moreover, to study the resolution effects on the extracted neutron multiplicities the mass distribution was folded with a Gaussian resolution function with a standard deviation of two and four mass units, respectively. The  $\sigma_A = 2$  u value is a realistic resolution, whereas  $\sigma_A = 4$  u is an exaggerated value in our case. Similar resolution conditions of  $\sigma_E = 0.5$  and 5 MeV were posed on the single fragment distribution, which corresponds to a summed resolution of 1.4 and 7.1 MeV in the TKE distributions.

The simulated ratios of coincidence-to-noncoincidence mass and TKE distributions are depicted in Fig. 7. The ideal  $\bar{v}(A)$  data points correspond to the distributions with applied kinematic cuts [ $\cos(\vartheta) \geq 0.99$ ,  $\cos(\theta_{c.m.}) \geq 0.0$  and  $E_n = 0.7$  MeV]. It reproduces the GEF  $\bar{v}(A)$  data (full lines labeled as ‘‘Input’’), within statistical uncertainty. This confirms the validity of the applied method, despite several kinematic cuts introduced in the data. The resolution smearing was applied to both coincidence and noncoincidence mass yields. The impact of  $\sigma_A = 2$  is small, whereas with  $\sigma_A = 4$ , the simulated  $\bar{v}(A)$  is significantly affected, causing a decrease in the three slopes of  $\partial\bar{v}(A)/\partial A$ . The  $\bar{v}(\text{TKE})$  seems resilient to the resolution effect at 0.5 MeV smearing (in each fragment energy), since it lacks structure and is rather smooth. However, at a magnified value of 5 MeV, the  $Q$ -value limit is violated and the slope clearly changed. The realistic experimental mass resolution is about  $\sigma_A = 2.3$  u and the energy resolution is about  $\sigma_E = 0.5$  MeV.

Lastly, two important corrections are needed as mentioned earlier, one for the backward-emitted neutrons [backward region in Fig. 5(b)] and another for the neutron center-of-mass

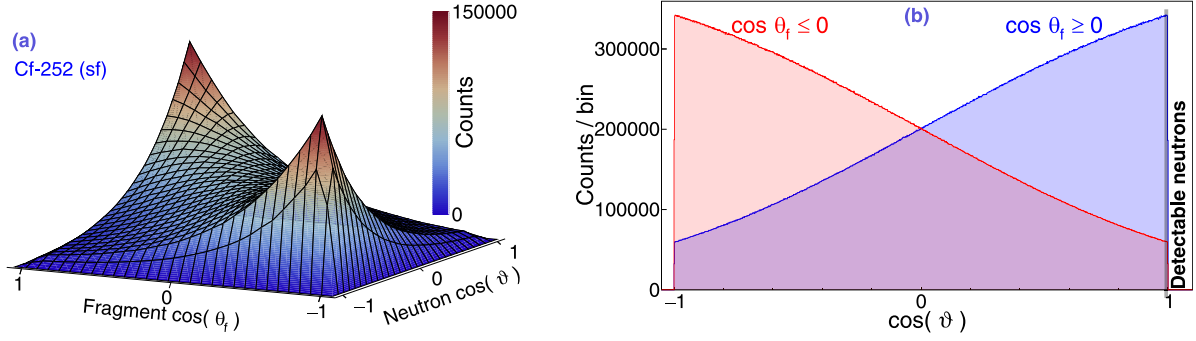


FIG. 4. Simulated fission data of fragments and neutrons for  $^{252}\text{Cf}(\text{sf})$ . (a) The correlation between the cosine of the fragment angle ( $\theta_f$ ) and the cosine of the neutron angle ( $\vartheta$ ), relative to the neutron detector symmetry axis. (b) The individual neutron  $\cos(\vartheta)$  distributions for the FF flying to the left and right hemispheres of the chamber. The tiny gray shaded area to the right highlights the detectable neutrons for one simulated detector.

angle  $\theta_{c.m.}$  [forward region in Fig. 5(b)]. The impact of these corrections can be studied in Fig. 8. The influence of the  $\theta_{c.m.}$  cut is depicted by the red dashed line. It overestimates the light fragment neutron yields and fails to reach the high neutron yields for very heavy FF. The impact of the neutrons from the complementary fragment (FF2) can be seen by the magenta dashed line. These neutrons are misidentified during the experiment to be emitted from FF1. This misidentification leads to the  $\bar{\nu}(A)$  values plotted in circles. Failing to correct for these effects, introduce severe errors in the deduced  $\bar{\nu}(A)$  values, plotted in blue symbols.

#### IV. EXPERIMENTAL DATA ANALYSIS

The experimental FF data were analyzed using the so-called 2-E technique where pre-neutron masses are calculated iteratively, based on known prompt-fission neutron multiplicities [10,25,26]. The neutron multiplicity is obtained via the ratio of the two mass distributions, with and without coincidence restriction with the neutron detectors (see Sec. III B).

The detector pulses from the digital acquisition were stored for off-line analysis and one event is illustrated as an example in Fig. 9. The cathode signal is used to trigger the fission event, followed by a neutron detector signal and the other chamber signals. The TOF is calculated between the cathode and either of the NDs.

#### A. Analysis of neutron data

In order to retrieve the fission neutrons, they have to be distinguished from other neutrons, prompt-fission  $\gamma$  rays as well as other background  $\gamma$  rays. The  $^{252}\text{Cf}(\text{sf})$  reaction was used to determine the detector efficiencies, which were then used in the data analysis for the  $^{235}\text{U}(n_{\text{th}}, f)$  reaction.

Figure 10 depicts the different stages of the neutron data analysis. The prompt-fission neutrons were separated from  $\gamma$  rays by means of a traditional pulse-shape (PS) discrimination analysis, utilizing the zero crossover method [23]. In Fig. 10(a) the pulse shape (zero-crossing) is plotted versus the pulse height from the photomultiplier tube. Gaussian distributions were fitted in intervals as a function of ND pulse

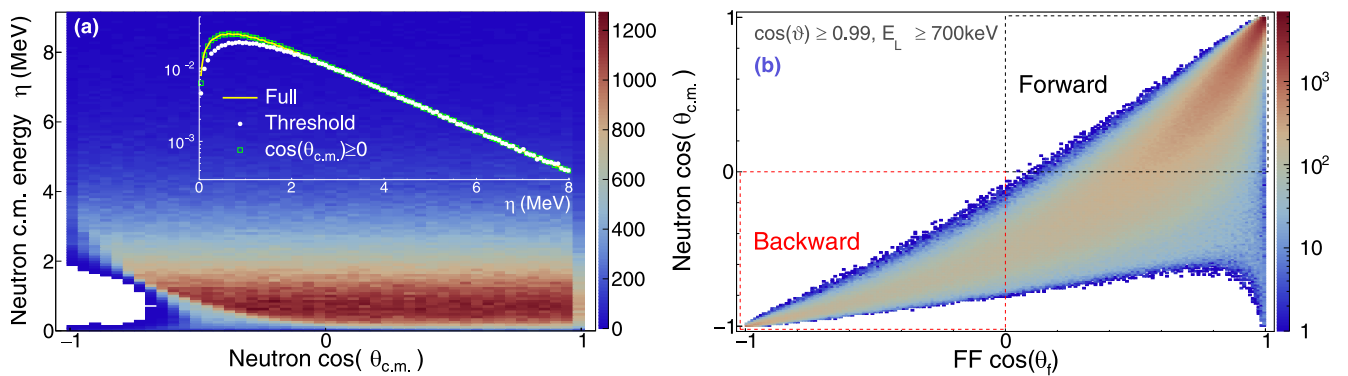


FIG. 5. (a) The neutron energy in the center-of-mass system,  $\eta$ , versus neutron  $\cos(\theta_{c.m.})$  distribution. The cut at lower cosine values is caused by the detector threshold of  $E_n = 0.7$  MeV. The inset shows the projection on the  $y$  axis. The neutron spectrum is altered by the intrinsic threshold and is restored by the kinematic cut [ $\cos(\theta_{c.m.}) \geq 0$ ]. (b) The simulated fission neutron detection in one neutron detector, as contributed from both FF. The forward region highlights the neutrons after the cut in the emitting fragment reference frame. The backward region, instead, highlights the neutrons from backward-flying FF [ $\cos(\theta_f) \leq 0$ ] arriving at the detector. The backward data is treated as a perturbation, which requires a correction [10].

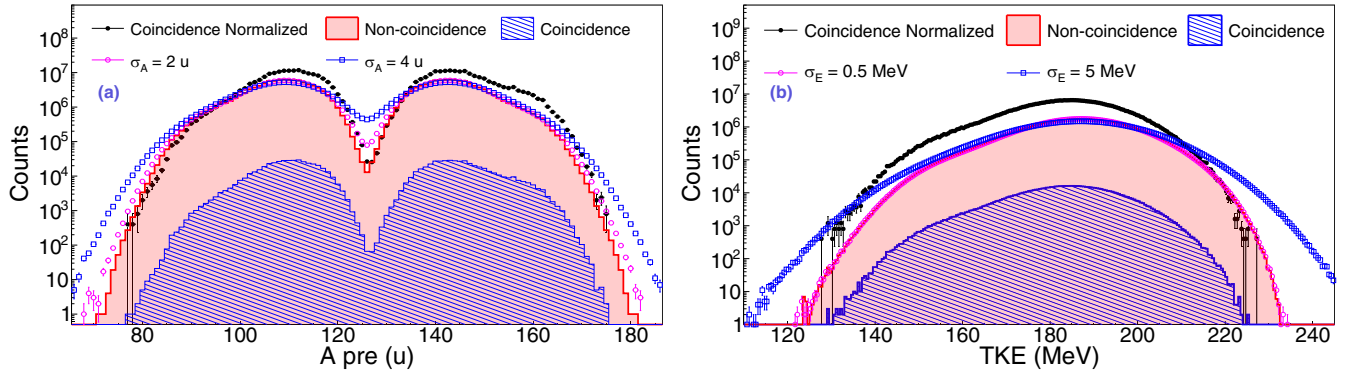


FIG. 6. GEF simulations from  $^{252}\text{Cf}(\text{sf})$ . (a) The mass distributions, with and without neutron coincidence condition [ $\cos(\vartheta) \geq 0.99$ ,  $\cos(\theta_{\text{c.m.}}) \geq 0.0$  and  $E_n = 0.7$  MeV]. The coincidence distribution was corrected for the geometrical efficiency. (b) The simulated TKE distributions, with and without neutron coincidence condition. The impact of mass and energy resolution is also studied, assuming values of  $\sigma_A = 2$  and  $4$  u and  $\sigma_E = 0.5$  and  $5$  MeV.

height, to the  $\gamma$  ray and neutron peaks. The midpoints between the two mean peak positions were selected to separate photons and neutrons, via a four-degree polynomial fit [seen in Fig. 10(a)]. Unrealistically high values due to pileup, were discriminated by a fit to the  $5\sigma_n$  values, where  $\sigma_n$  is the standard deviations of the Gaussian fits to the neutron peaks. The time-of-flight (TOF) distribution is shown in Fig. 10(b), and was obtained from the time difference between the constant fraction discriminated (CFD) signals from the cathode and the neutron detector, respectively. The time calibration was performed using the known position of the prompt-fission  $\gamma$  peak. The TOF was corrected for remaining walk effects resulting from variations in the cathode signal height. The timing resolution was estimated by fitting a Gaussian distribution to the prompt-fission  $\gamma$  peak in  $^{252}\text{Cf}(\text{sf})$ , and was found to be  $1.3$  ns full width at half maximum (FWHM). To discriminate the remaining contribution from prompt-fission  $\gamma$  rays, instead of a sharp threshold in TOF, a pulse-height-dependent cut was applied, exploiting the kinematics of the (n,p) scattering in the liquid scintillator [24]:

$$\text{TOF} \geq d[2L/\cos(\tau)]^{-1}, \quad (3)$$

where  $d$  is the flight distance,  $L$  is the calibrated light output pulse height, and  $\tau$  is the proton scattering angle. A  $\cos(\tau)$  value of  $0.15$  was selected to discriminate the prompt  $\gamma$  rays from neutrons. The kinematic cut based on Eq. (3) is shown by the dashed line in Fig. 10(c). The detector pulse-height calibration was performed with standard  $\gamma$ -ray sources ( $^{137}\text{Cs}$  and  $^{22}\text{Na}$ ), to obtain the electron equivalent light output (MeVee). In addition to the lower light output threshold, an upper limit was also imposed through a dynamical light output cut [24]. The upper limit was set at the maximum proton energy for a given neutron energy plus  $2\sigma$ , referring to the light output resolution. The upper limit values were fitted with the functional dependency used in Ref. [17]:

$$L(E_p) = \frac{L_0 E_p^2}{E_p + L_1} + L_2, \quad (4)$$

where  $L_i$  are free fit parameters. The dashed line in Fig. 10(d) shows the fit to the upper limit values, whereas the solid line is the fit to the  $L + 2\sigma$  values. The fit was used to filter out unrealistic  $L(E_p)$  values for a given neutron energy. The final TOF distribution for the fission neutrons, including a light

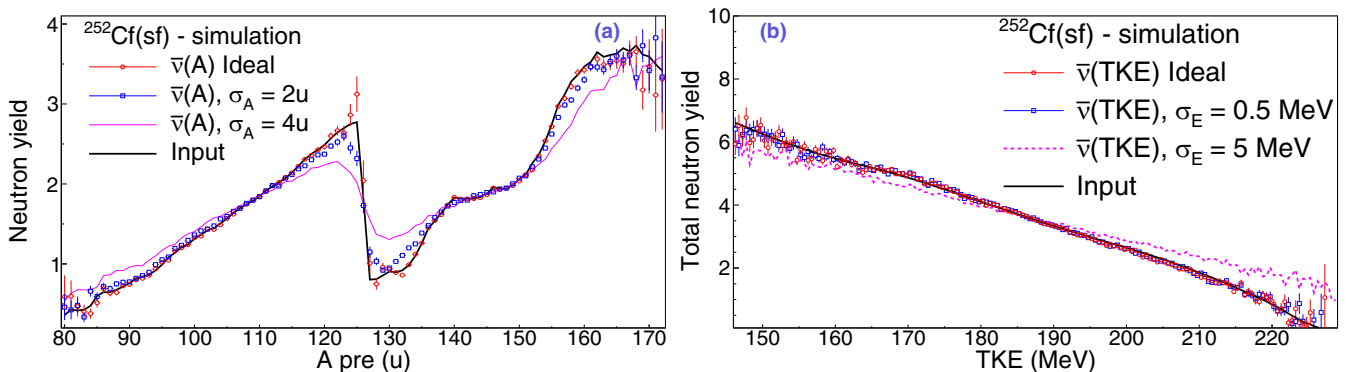


FIG. 7. The simulated detection of prompt-fission neutrons as a function of (a) fragment mass and (b) total kinetic energy. The neutron multiplicity is obtained by the coincidence condition [ $\cos(\vartheta) \geq 0.99$ ,  $\cos(\theta_{\text{c.m.}}) \geq 0.0$  and  $E_n = 0.7$  MeV] between the fission detector and the neutron detector. The resulting curves (labeled “Ideal”) reproduce the GEF data (labeled “Input”) well. The impact of mass and energy resolution is also studied, assuming values of  $\sigma_A = 2$  and  $4$  u and  $\sigma_E = 0.5$  and  $5$  MeV.

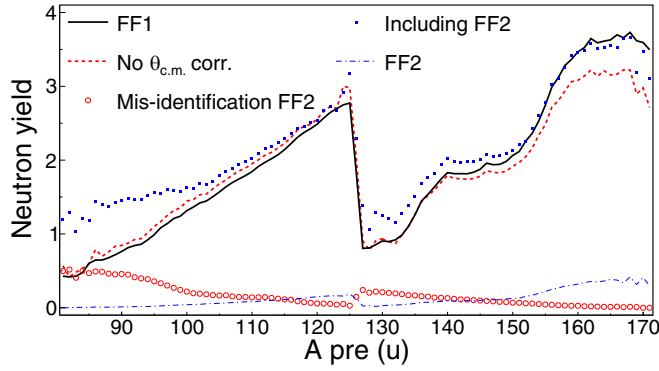


FIG. 8. The impact of data corrections on the original  $\bar{\nu}(A)$  for FF1 (black line). Without a cut on  $\theta_{c.m.} \leq 90^\circ$ , the shape is altered, mostly for heavier masses as seen by the red dashed line. The neutron contribution from the complementary fragment (FF2) is plotted in dash-dotted blue line. The mis-identification of the emitting nucleus of these neutrons is inevitable during the experiments, which leads to a background (red open circles). Failing to correct for these backward-emitted neutrons influences the deduced shape severely (blue rectangle symbols).

output threshold of 0.1 MeVee, is highlighted in Fig. 10(b) (transparent green filled histogram).

Once the neutron TOF distributions are derived, the internal detector efficiency can be calculated. For that, the Mannhart neutron spectrum evaluation, plotted in Fig. 11, comes to the rescue [27]. The measured neutron spectra are normalized for the geometrical efficiency, to the total number of prompt neutrons in  $^{252}\text{Cf}(\text{sf})$ ,  $\bar{\nu}_{\text{tot}} = 3.759$ , and to the total number of collected fission events. The intrinsic efficiency of the detectors were determined to be about 30–40 % around 1–2 MeV neutron energy, for a detector threshold of 0.1 MeVee. The detectors have a rather high intrinsic threshold at  $E_n \approx 0.7$  MeV, but this is not a problem as discussed in Sec. III B: The neutrons are predominantly emitted from fully

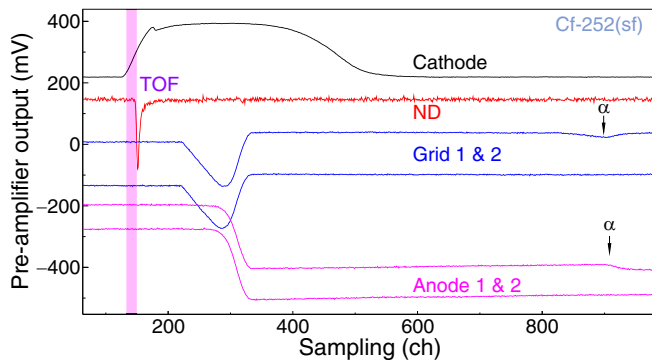


FIG. 9. Typical raw detector signals recorded with the digital acquisition system. The data from one neutron detector is shown (red) together with the pulses from anodes (magenta), grids (blue), and cathode (black). The signals also exhibit an  $\alpha$  pile-up in one chamber side, which was removed during off-line analysis. The time-of-flight (TOF) was determined from an off-line trigger to the cathode (start) and the neutron (stop) signals. The indicated TOF region highlights the time difference between the pick-off signals.

accelerated fragments, and we only consider neutrons above the average fragment energy/nucleon. This is guaranteed by a kinematic selection in emission angle relative to the fission axis [ $\cos(\theta_{c.m.}) \geq 0.0$ ].

### B. Analysis of the fission fragment data

The digital pulses from the anodes and grids were treated following the recipe of Refs. [13,26]. The signals were adjusted for baseline fluctuations, time drifts, and corrected for  $\alpha$  pileup (an example of pileup produced by an  $\alpha$  particle is shown in Fig. 9). The total signal generated on the anode plate,  $Q_A$ , is proportional to the number of ion-electron pairs liberated in the ionization process,  $n_0$ , and thus to the fragment postneutron emission energy ( $E_{\text{post}}$ ). Due to an inefficiency in the shielding by the grid, a small correction is needed to extract the full signal height:

$$Q_A = -n_0 e + \sigma n_0 e \frac{\bar{X}}{D} \cos(\theta_f) \propto E_{\text{post}}, \quad (5)$$

where  $\bar{X}$  is the center of gravity of the electron-cloud distribution,  $D$  is the cathode-grid distance (31 mm), and  $\sigma = 0.031$  denotes the grid inefficiency magnitude, which was corrected for according to Refs. [29,30]. The grid signal height,  $Q_G$ , has a stronger dependence on the fragment emission angle:

$$Q_G = n_0 e (1 - \sigma) \frac{\bar{X}}{D} \cos(\theta_f), \quad (6)$$

The FF angular distributions were deduced by utilizing the grid pulse height directly and by determining  $\bar{X}/D$  as a function of pulse height (with a second-order correction for the mass dependence) [28]. The energy losses were corrected for as a function of  $\cos(\theta_f)$ , as can be seen in Fig. 12.

The FF energies were adjusted for the pulse height defect (PHD), caused by recombination effects and nonionizing interaction in the counting gas. The effect amounts to about 2–5 MeV and was parameterized as in Ref. [31]:

$$E_{\text{phd}}(A_{\text{post}}, E_{\text{post}}) = A_{\text{post}} \left( \frac{E_{\text{post}}}{\alpha} + \frac{1}{\beta} \right). \quad (7)$$

The parameters  $\alpha$  and  $\beta$  were calibrated for the  $^{252}\text{Cf}(\text{sf})$  reaction to allow for a reproduction of known literature values for TKE and  $\langle A_{\text{pre}} \rangle$  [32]. The calibrated values were then used for the  $^{235}\text{U}(\text{n}_{\text{th}}, \text{f})$  reaction. Once the postneutron energies are calibrated, they can be used to calculate the preneutron emission mass distributions, which are given by the compound nuclear mass ( $A_{\text{CN}}$ ) and the fragments' preneutron emission kinetic energies:

$$A_{1,2}^{\text{pre}} = A_{\text{CN}} \cdot E_{2,1}^{\text{pre}}(\text{TKE})^{-1}, \quad (8)$$

where the indices 1 and 2 denote the two fragments. In order to calculate the mass on an event-by-event basis, an iterative procedure is followed, which involves an initial mass guess and external input data on  $\bar{\nu}(A)$  [4,33]. The preneutron emission energy in the laboratory system can be calculated as:

$$E_{\text{pre}} \approx \frac{A_{\text{pre}}}{A_{\text{pre}} - \bar{\nu}(A, \text{TKE})} E_{\text{post}}. \quad (9)$$

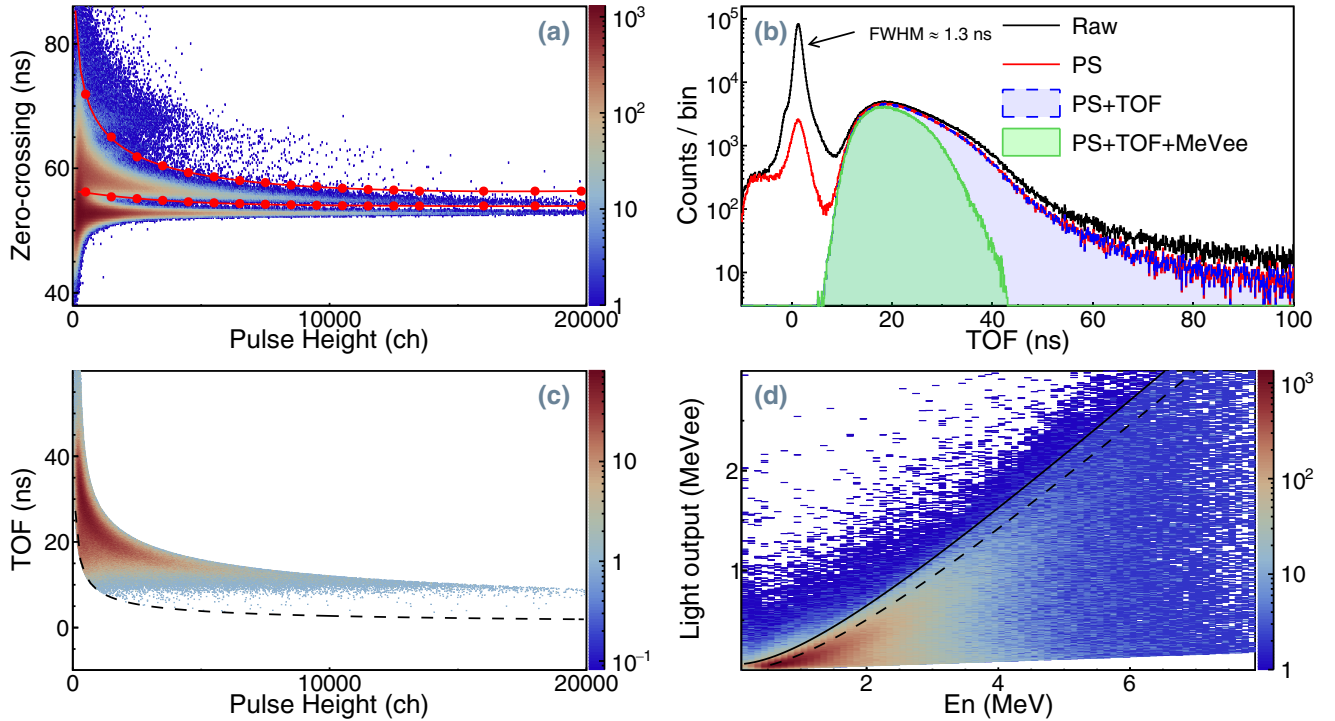


FIG. 10. (a) The liquid scintillator pulse shape (zero crossover method [23]) versus pulse height for  $^{252}\text{Cf}(\text{sf})$ , together with the polynomial fits to discriminate neutrons and  $\gamma$  rays. (b) The time-of-flight (TOF) of the neutrons between the fission source at the cathode electrode and the ND. The timing resolution is about 1.3 ns in FWHM. The impact of PS discrimination is seen by the black (labeled with the FWHM value) and red (after correction) lines. The fission-neutron TOF contribution, after the TOF cut, is drawn in blue dashed line. The green shaded area, with full border line, highlights the final neutron TOF distribution with an applied threshold of 0.1 MeV electron equivalent. (c) The pulse height dependent TOF cut following Eq. (3). (d) Fits to the maximum proton recoil (dashed line) as well as a fit to the  $L + 2\sigma$  values (solid line), to apply the dynamical light output cut following the functional dependency of Eq. (4) [24, p28].

The calibrated and iterated kinetic energies from the sample and backing sides are plotted in Fig. 13 for  $^{235}\text{U}(\text{n}_{\text{th}}, \text{f})$  and  $^{252}\text{Cf}(\text{sf})$ . In the 2-E technique, it is important to consider the neutron emission ( $\bar{\nu}$ ) to calculate the mass in Eq. (9). It depends mainly on the fragment mass and less on the total kinetic energy (TKE). For this purpose, either literature neutron yields are used or values are inferred from models [33]. We tested two different  $\bar{\nu}(A)$  data sets on  $^{235}\text{U}$  [8,11], in order to study the sensitivity of the final results on this choice. The results were practically unchanged with respect to the choice of data and the final results presented here were obtained with the evaluated data from Wahl [8]. The TKE dependence was parameterized as:

$$\nu(A, \text{TKE}) = \bar{\nu}(A) + \frac{\bar{\nu}(A)}{\bar{\nu}(A) + \bar{\nu}(A_{\text{CN}} - A)} \frac{\overline{\text{TKE}}(A) - \text{TKE}}{E_{\text{sep}}}, \quad (10)$$

where  $E_{\text{sep}} = 8.6$  MeV the energy needed to emit a neutron and  $\overline{\text{TKE}}(A)$  is the mean TKE as a function of fragments mass [37]. This parametrization of the neutron multiplicity is taken into account in the iterative calculation in order to determine the preneutron emission energy. The calculations above are repeated in a loop where the improved masses are always derived from masses from earlier steps. When the mass difference,  $A_{\text{new}} - A_{\text{old}}$ , is less than 0.1 u in two sequential iterations, the iteration is stopped and the FF mass is rounded

to nearest integer. To reduce the influence of events with large energy and angular straggling, a cut on FF emission angle,  $\cos(\theta_f) \geq 0.5$  was applied on the noncoincidence data [32]. This particular cut was not applied on the coincidence FF data because the kinematic boost already selects fragments with small  $\theta_f$  angles [see Fig. 5(b)]. Moreover, such a cut influences the neutron multiplicities by affecting the isotropic neutron angular distribution. This in turn leads to wrong  $\bar{\nu}(A)$  results, which was confirmed by the simulations.

### C. Determination of the neutron yields

The fission neutron energy in the laboratory frame ( $E_L$ ) can be transformed to the fragment center-of-mass system energy ( $\eta$ ) following Eq. (1). The measured distribution is plotted in Fig. 14 for  $^{235}\text{U}(\text{n}_{\text{th}}, \text{f})$  and  $^{252}\text{Cf}(\text{sf})$ , respectively. The prompt fission neutron spectra (PFNS) were calculated as the average of both neutron detectors, for each reaction. The PFNS were then fitted with the neutron evaporation cascade model, following the formula of Le Couteur and Lang (based on Weisskopf's statistical theory) with an effective nuclear temperature parameter ( $T_{\text{eff}}$ ) [38,39]:

$$\phi(\eta) = \eta^\lambda \exp(-\eta/T_{\text{eff}}) \quad . \quad (11)$$

The fitted parameter values were  $\lambda = (0.385 \pm 0.01)$  and  $T_{\text{eff}} = (1.031 \pm 0.007)$  MeV for  $^{252}\text{Cf}(\text{sf})$ , which are close



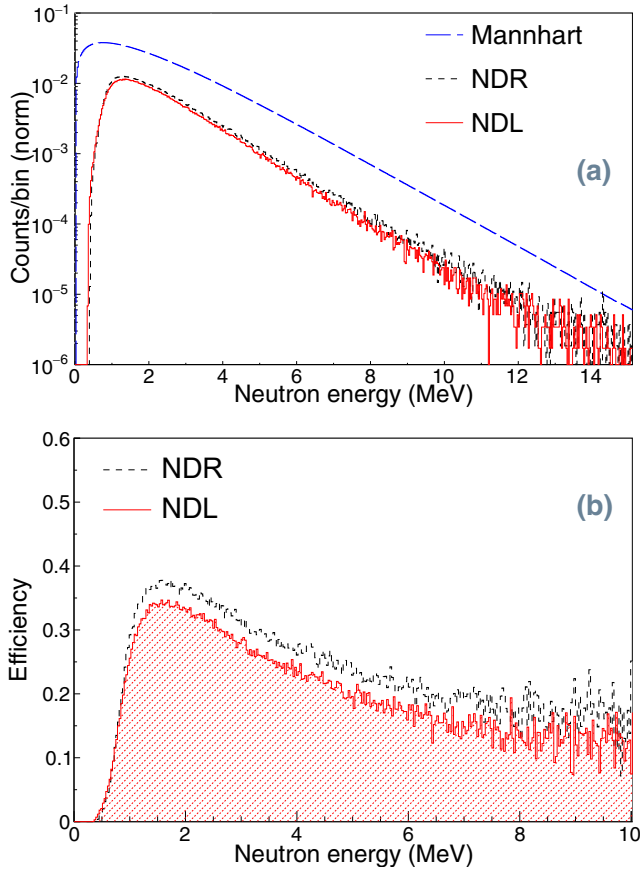


FIG. 11. (a) The  $^{252}\text{Cf}(\text{sf})$  neutron spectrum in the laboratory system, as measured in NDR and NDL. The Mannhart neutron-spectrum evaluation is taken as reference to calculate the internal detector efficiency [27]. (b) The detector efficiency (fraction of 1.0) of the detectors, calculated relative to the Mannhart evaluation. The determined efficiency from  $^{252}\text{Cf}(\text{sf})$  is later used for the  $^{235}\text{U}(\text{n}_{\text{th}}, \text{f})$  case.

to the values of Budtz-Jørgensen *et al.* ( $\lambda = 0.38$  and  $T_{\text{eff}} = 1.07$  MeV [10]) and SCINTIA ( $\lambda = 0.42$  and  $T_{\text{eff}} = 1.07$  MeV [11]). In the case of  $^{235}\text{U}(\text{n}_{\text{th}}, \text{f})$ , a Maxwellian was fitted (fixed value of  $\lambda = 0.5$ ), which gave a temperature of  $T_{\text{eff}} = (0.847 \pm 0.002)$  MeV, also in decent agreement with the value from SCINTIA ( $T_{\text{eff}} = 0.831$  MeV) [5]. As pointed out in Ref. [5], the deviation in  $^{235}\text{U}(\text{n}_{\text{th}}, \text{f})$  PFNS from the Maxwellian shape is mainly due to the contribution of light fragments.

The neutron spectrum is used to estimate the portion of back-emitted neutrons, from the complementary FF, hitting the neutron detector. As stressed earlier, the experimental mass distribution was determined with and without coincidence with the neutron detectors. In addition to the natural kinematic cut due to the limited solid angle coverage and the intrinsic neutron detector threshold, an angular cut was applied [ $\cos(\theta_{\text{c.m.}}) \geq 0.0$ ] to select only neutrons with higher energies than the fragment energy per nucleon (see Sec. III B). Despite the kinematic boost, a small fraction of neutrons from the complementary fragment arrive to the opposite detector, as was shown earlier. In order to correct for this perturbation, we

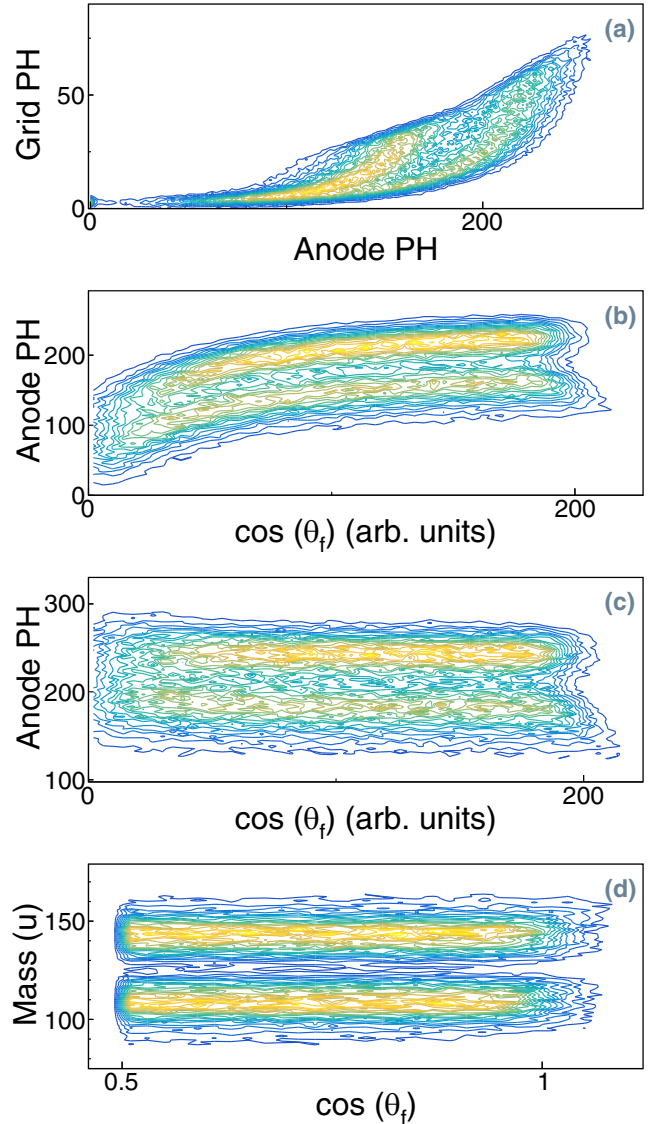


FIG. 12. (a) The anode versus grid pulse heights, from the backside of the  $^{252}\text{Cf}(\text{sf})$  target. The length of the distribution along the y axis contains the information on  $\bar{X}/D$ . The pulse height as a function of fragment emission angle,  $\cos(\theta_f)$ , is shown before (b) and after (c) energy-loss correction. (d) The mass dependence of  $\bar{X}/D$  is also corrected for (see Ref. [28] for details).

calculate the probability of neutron emission from both fragments, on an event-by-event basis [10,11]. First, the neutron recoil to the fragment has to be taken into account in Eq. (9), for coincidence events:

$$E_{\text{pre}}^{\text{coinc}} = \frac{A_{\text{pre}}}{A_{\text{pre}} - \nu(A_{\text{pre}}, \text{TKE})} E_{\text{post}} \pm \frac{2E_{\text{pre}}}{A_{\text{pre}}} \left( \sqrt{\frac{E_L A_{\text{pre}}}{E_{\text{pre}}}} \cos(\theta_L) - 1 \right), \quad (12)$$

where the + (−) sign corresponds to the fragment flying away from (towards) the detector [40]. For each neutron event, the probability of forward ( $\epsilon$ ) and backward ( $\epsilon^*$ ) emission is

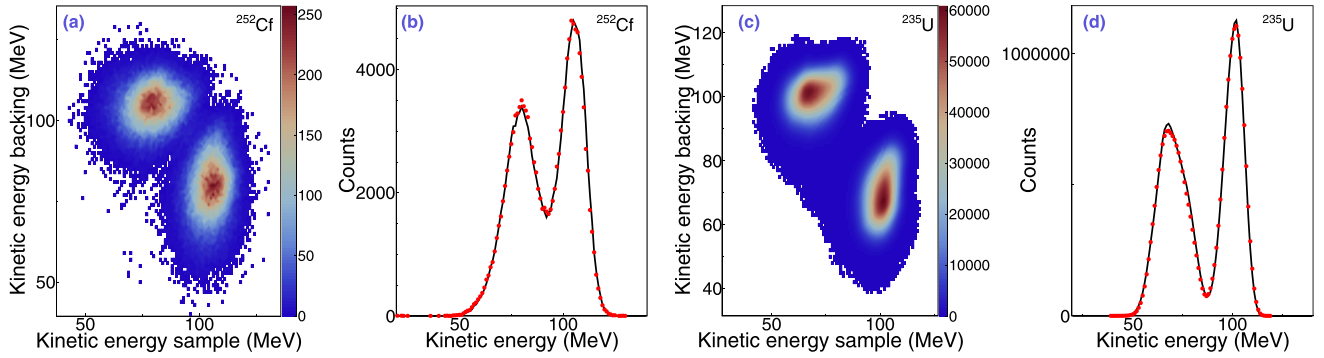


FIG. 13. The kinetic energy distributions for  $^{252}\text{Cf}(\text{sf})$  in (a), (b) and  $^{235}\text{U}(\text{n}_{\text{th}}, \text{f})$  in (c), (d). In (a) and (c), the energies from sample side are plotted versus the energies from backing side. The projections of the two-dimensional distributions are plotted in (b) and (d). The energies from sample and backing sides are in good agreement.

calculated for both FF. The forward emission efficiency,  $\epsilon$ , is assumed to equal to all neutrons hitting the detector, because the vast number of neutrons hitting the detector do originate from forward-flying FF. The backward emission efficiency is calculated from the ratio of the center-of-mass energies ( $\eta'$  and  $\eta$ ):

$$\epsilon^* = \epsilon \left( \frac{\eta'}{\eta} \right)^\lambda \exp \left( -\frac{\eta' - \eta}{T_{\text{eff}}} \right), \quad (13)$$

where  $\eta$  ( $\eta'$ ) is the neutron energy assuming an emission from the fragment flying towards (away from) the detector. Based on the calculated probabilities, the coincidence mass distributions can be weighted with each of  $\epsilon'$  and  $\epsilon$ . Figure 15 shows these weighted mass distributions from one detector, for  $^{252}\text{Cf}(\text{sf})$  [Fig. 15(a)] and  $^{235}\text{U}(\text{n}_{\text{th}}, \text{f})$  [Fig. 15(b)], respectively. The neutron yields from backward-emitting fragments are much smaller compared to the forward ones. The final mass data are corrected for this perturbation by subtracting the contribution of neutrons emitted in backward direction. The correction is typically several percent for most probable masses. However, due to the strong asymmetry in the sawtooth shape, the correction is larger for other masses as shown by the plotted ratio of backward-to-forward distributions in Fig. 15. For instance, for masses around  $A_{\text{pre}} \approx 130$  the correction may

reach 10–20 % (see also Ref. [11]). The final prompt-fission neutron yields were corrected for the geometrical efficiency and then scaled to the ENDF-B-VIII.0 evaluated total prompt-neutron multiplicities,  $\bar{\nu}_{\text{tot}} = 3.759$  in  $^{252}\text{Cf}(\text{sf})$  and 2.414 in  $^{235}\text{U}(\text{n}_{\text{th}}, \text{f})$ .

## V. RESULTS

A summary of the counting statistics is given in Table I. Due to the difference in acquisition system trigger scheme, the majority of acquired events are ND + TFGIC coincidences in the case of  $^{252}\text{Cf}(\text{sf})$ , in contrast to  $^{235}\text{U}(\text{n}_{\text{th}}, \text{f})$ , where the physical trigger came from the chamber itself [see Fig. 1(b)]. In the following we investigate the performance of the two neutron detectors, the ionization chamber and finally the coincidence data of both detector systems.

### A. Mass and TKE distributions

The mass yields and two-dimensional mass versus TKE distributions, resulting from  $^{252}\text{Cf}(\text{sf})$  and  $^{235}\text{U}(\text{n}_{\text{th}}, \text{f})$ , are displayed in Figs. 16, 17, and 18. The Y(A) data are compared to three data sets in case of  $^{252}\text{Cf}(\text{sf})$  [10,11,34] (from the same facility and using the same technique) and three different data sets in case of  $^{235}\text{U}(\text{n}_{\text{th}}, \text{f})$  [5,35,36]. For  $^{252}\text{Cf}(\text{sf})$ , the mass

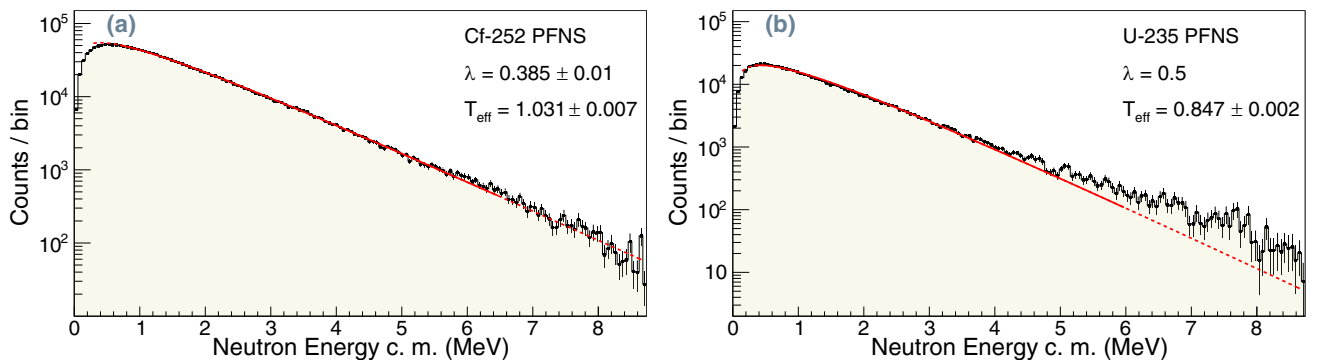


FIG. 14. The measured average prompt fission neutron spectra (PFNS) for the two reactions, in the rest frame of the emitting fission fragment. Both PFNS were fitted with the statistical neutron evaporation cascade model [Eq. (11)]. The data have been corrected for the contribution of backward neutron emission [Eq. (13)].

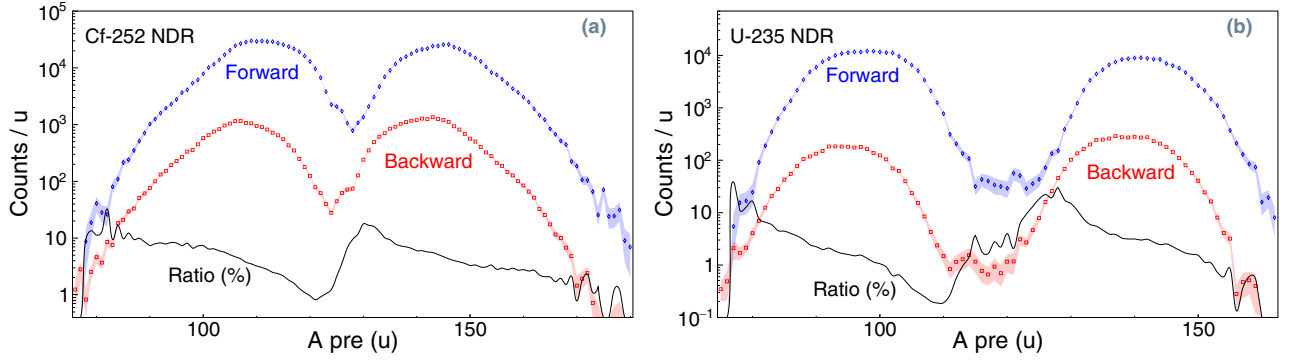


FIG. 15. The contribution from forward [efficiency weight ( $\epsilon$ )] and backward ( $\epsilon^*$ ) neutron-fragment coincidences, as detected in coincidence by the TFGIC and NDR. For  $^{252}\text{Cf}(\text{sf})$  in (a) for  $^{235}\text{U}(\text{n}_{\text{th}}, \text{f})$  in (b). The ratio of backward to forward distributions is also plotted, which demonstrates the size of the applied correction for the contribution of backward emitted neutrons. The color bands illustrate the statistical uncertainties.

distribution is in fair agreement to the other data. The peak-to-valley ratio is about 20 for  $^{252}\text{Cf}(\text{sf})$  and the heavy fragment group has an average value of  $\langle A_{\text{pre,H}} \rangle = (143.55 \pm 0.02)$ . A slightly lower peak-to-valley ratio is obtained as compared to Refs. [11,34]. This is likely caused by a slightly lower mass resolution, owed to a worse homogeneity of the californium layer as stressed in Ref. [41].

In the case of  $^{235}\text{U}(\text{n}_{\text{th}}, \text{f})$ , the agreement to the other literature data is excellent, especially to the recent epithermal data of JRC. The peak-to-valley ratio is 470 and the  $\langle A_{\text{pre,H}} \rangle$  is  $(139.455 \pm 0.001)$ . The experimental mass resolution in case of  $^{235}\text{U}(\text{n}_{\text{th}}, \text{f})$  was estimated by comparison to the high-resolution yield data of Geltenbort *et al.* [36]. The data was convoluted with a Gaussian resolution function with a standard deviation of  $\sigma_A = 2.3$  u, and the resulting distribution reproduced our  $Y(A)$  data very well, as can be seen in Fig. 17(b).

The TKE versus preneutron emission mass distribution for  $^{252}\text{Cf}(\text{sf})$  is shown in Fig. 18(a), and was calibrated to reproduce the recommended mean total kinetic energy of  $(184.1 \pm 1.3)$  MeV [42]. The  $\overline{\text{TKE}}(A)$  data agrees with SCINTIA in general, especially in the regions of high fragment yields. However, the dip in the symmetry region is not fully reproduced, but follows better the data of Budtz-Jørgensen *et al.* [10]. The higher average TKE for symmetric splits arises from spurious events caused by the lower quality of the californium sample, as stressed earlier, hence giving higher symmetric yields and  $\overline{\text{TKE}}$ . No sign of a similar effect was found in case of  $^{235}\text{U}(\text{n}_{\text{th}}, \text{f})$  [see Fig. 18(b)] since the sample has a much better quality (homogeneity in the backing material). The  $\overline{\text{TKE}}(A)$  for  $^{235}\text{U}(\text{n}_{\text{th}}, \text{f})$  was also calibrated to the recommended literature value ( $\overline{\text{TKE}} = 170.5 \pm 0.5$ ) MeV

TABLE I. The counting statistics of the experiments. The tabulated number of coincidence events are for each neutron detector.

Nuclide	Noncoincidence	Coincidence (2 ND)
$^{252}\text{Cf}(\text{sf})$	$3 \times 10^5$	$9 \times 10^5$
$^{235}\text{U}(\text{n}_{\text{th}}, \text{f})$	$6 \times 10^7$	$3 \times 10^5$

[42]. The commonly known, yet startling, strong correlation between  $\overline{\text{TKE}}$  and the FF mass is attributed to variations in the deformation of the fissioning nucleus. Large  $\overline{\text{TKE}}(A_{\text{pre}})$  values around  $A_{\text{pre}} \approx 132$  are associated with a rather short neck between the two FF and thus a stronger repulsion, whereas symmetric mass splits exhibit long necks and, therefore, a dip of about 20 MeV in average kinetic energy. At larger mass asymmetry, the  $\overline{\text{TKE}}(A_{\text{pre}})$  also reduces strongly compared to  $A_{\text{pre}} \approx 132$ , partly due to an increasing distance between FF centers and partly due to reducing  $Z_1 \times Z_2$  values in the Coulomb repulsion.

## B. Neutron yields as a function of mass and TKE

### 1. Comparison of the two neutron detectors

The  $\bar{\nu}(A)$  results for  $^{252}\text{Cf}(\text{sf})$  are plotted in Fig. 19(a) for both neutron detectors and in comparison to results from SCINTIA [5]. The overall features of the fission-neutron multiplicity agree, for instance the positions of the low multiplicity values around  $A_{\text{pre}} \approx 80$  and 130, and we see a steady increase towards  $A_{\text{pre}} \approx 124$  and 170. The data from the two detectors are in good agreement around the most probable masses, but some differences are observed at the wings of the mass distribution, where statistics drop drastically. For mass numbers between  $A_{\text{pre}} \approx 85$  and 100, the data from NDR seem to reproduce the shoulder rather well, in contrary to ND. This behavior is reversed for masses heavier than  $A_{\text{pre}} = 155$ , where ND seems to agree better with the literature data. These discrepancies may be attributed to the quality of the  $^{252}\text{Cf}(\text{sf})$  sample, which affects the energy and angular straggling and thus the extracted  $\bar{\nu}(A)$  [41], especially at the wings of the mass distribution [34]. From the distributions we also extract the average neutron emission from the light and heavy fragments, respectively. For NDR the mean values are:  $\bar{\nu}_{\text{tot,L}} \approx 2.08$  and  $\bar{\nu}_{\text{tot,H}} \approx 1.68$ . The corresponding values for ND are:  $\bar{\nu}_{\text{tot,L}} \approx 2.00$  and  $\bar{\nu}_{\text{tot,H}} \approx 1.75$ . The  $\bar{\nu}(\text{TKE})$  data for  $^{252}\text{Cf}(\text{sf})$  is plotted in Fig. 19(b) and are internally consistent. Some deviation from linearity is observed at very low TKE values, where statistics is low. Due to a smaller yield at low TKE, data show generally large uncertainties in this region, as discussed more extensively in Ref. [5].

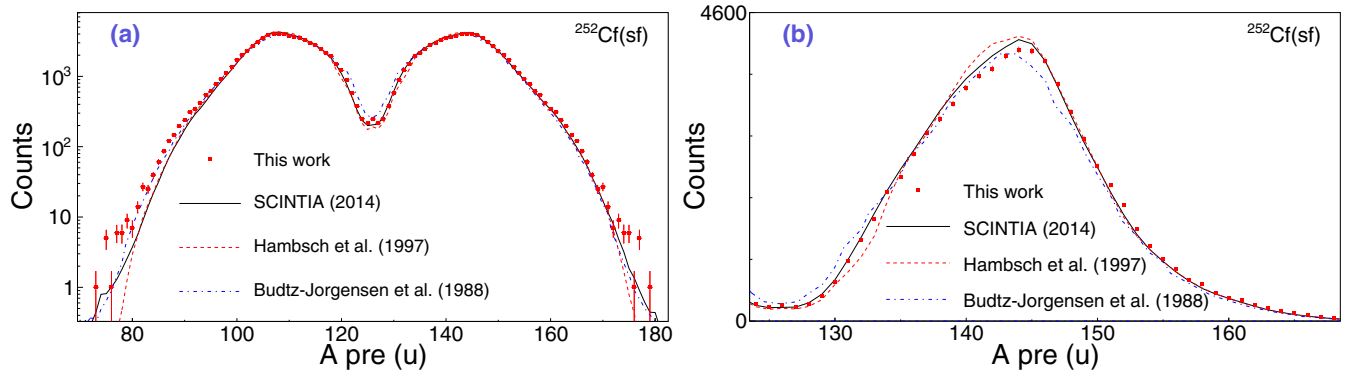


FIG. 16. The preneutron emission mass yields for  $^{252}\text{Cf}(\text{sf})$  in (a) logarithmic and (b) linear scales. The literature data [10,11,34] has been normalized to the total yield of this work.

The results for  $^{235}\text{U}(\text{n}_{\text{th}}, \text{f})$  are shown in Fig. 19(c) for  $\bar{\nu}(A)$  and in Fig. 19(d) for  $\bar{\nu}(\text{TKE})$ . The data from the two detectors exhibit much smaller differences compared to the  $^{252}\text{Cf}(\text{sf})$  case, and they reproduce the SCINTIA epithermal data very well. The values at most probable masses are internally consistent and the position of the minimum caused by double magicity, is found around  $A_{\text{pre}} \approx 128$ . One exception to the excellent agreement is, however, masses in the vicinity of  $A_{\text{pre}} \approx 110$ . The reason for the discrepancy in this particular region is not fully understood, but one possible explanation (albeit unlikely) is the difference between thermal and epithermal energies and the presence of resonances in the fission cross section. The SCINTIA data, however, has higher statistics in the symmetry region and in addition a slightly better mass resolution, due to the use of a position sensitive anode in the TFGIC. A more likely explanation for the discrepancy is a resolution effect, which washes out the  $\bar{\nu}(A)$  values for symmetric mass, similarly to the effect encountered in the simulations and shown in Fig. 7(a). The impact of such resolution effect is exaggerated at those masses, since the yield is rather low. For  $^{235}\text{U}(\text{n}_{\text{th}}, \text{f})$ , the results from NDR give rise to the mean values  $\bar{\nu}_{\text{tot,L}} \approx 1.41$  and  $\bar{\nu}_{\text{tot,H}} \approx 1.00$ . The corresponding values for NDL were  $\bar{\nu}_{\text{tot,L}} \approx 1.39$  and  $\bar{\nu}_{\text{tot,H}} \approx 1.03$ . The  $\bar{\nu}(\text{TKE})$  data for  $^{235}\text{U}(\text{n}_{\text{th}}, \text{f})$  agree both internally between the two detectors as well as with the SCINTIA results. This is to some extent expected, because

the fission dynamics should be fairly similar at thermal and epithermal incident neutron energies.

## 2. Comparison to literature data

The obtained average neutron-multiplicity data from both detectors are compared to literature data in Figs. 20 and 21. In the case of  $^{252}\text{Cf}(\text{sf})$ ,  $\bar{\nu}(A)$  is compared to data from Refs. [10,11,43]. The average prompt  $\bar{\nu}_{\text{tot}}$  values for light and heavy fragments are:  $\bar{\nu}_{\text{tot,L}} \approx 2.04$  and  $\bar{\nu}_{\text{tot,H}} \approx 1.72$ , confirming literature data within 1% (2.056/1.710 [22]). The  $\bar{\nu}(\text{TKE})$  for  $^{252}\text{Cf}(\text{sf})$  is compared to data from Refs. [5,10]. The change in  $\overline{\text{TKE}}$  as a function of total neutron emission was deduced by a linear fit to the data. The fit resulted in a value of  $\partial \overline{\text{TKE}} / \partial \bar{\nu} = (-12.9 \pm 0.2)$  MeV/n, which is within statistical uncertainty limits of the reported SCINTIA value  $(-12.6 \pm 0.2)$  MeV/n [11] and Budtz-Jørgensen *et al.* [10]  $(-12.5)$  MeV/n.

In the case of  $^{235}\text{U}(\text{n}_{\text{th}}, \text{f})$ ,  $\bar{\nu}(A)$  is compared to data from Refs. [5–7,9] and to the Wahl evaluation [8]. Both our and the epithermal SCINTIA data, hint to a shifted minimum from  $A_{\text{pre}} \approx 130$ –128. The data also show significant lower neutron multiplicities around  $A_{\text{pre}} = 80$  compared with the earlier data sets and evaluations. The average  $\bar{\nu}_{\text{tot}}$  values for light and heavy fragments are  $\bar{\nu}_{\text{tot,L}} \approx 1.40$  and  $\bar{\nu}_{\text{tot,H}} \approx 1.02$ , which are in close agreement with literature total

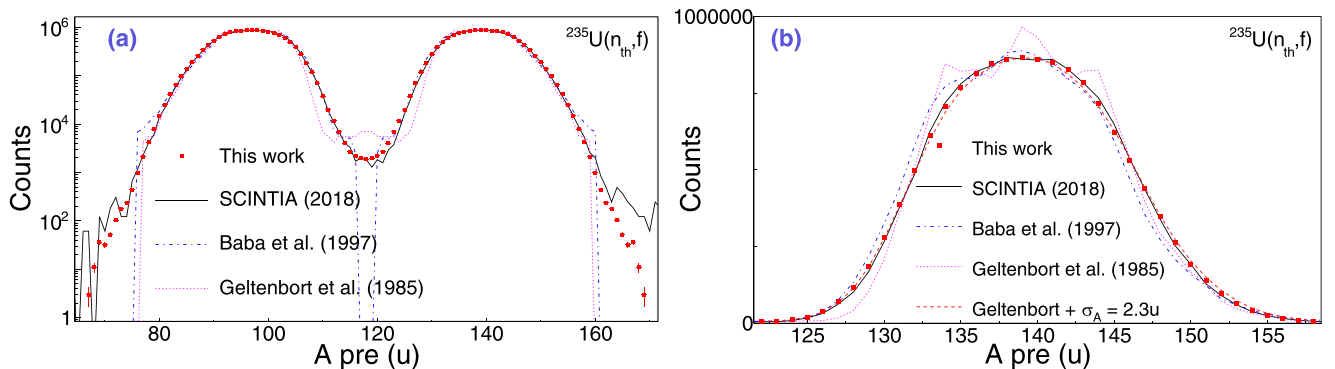


FIG. 17. The preneutron emission mass yields for  $^{235}\text{U}(\text{n}_{\text{th}}, \text{f})$  in (a) logarithmic and (b) linear scales. The literature data [5,35,36] has been normalized to the total yield of this work. The high-resolution data from Ref. [36] was used to estimate the mass resolution of this work, by folding the literature data with a Gaussian resolution function of  $\sigma_A = 2.3$  u.

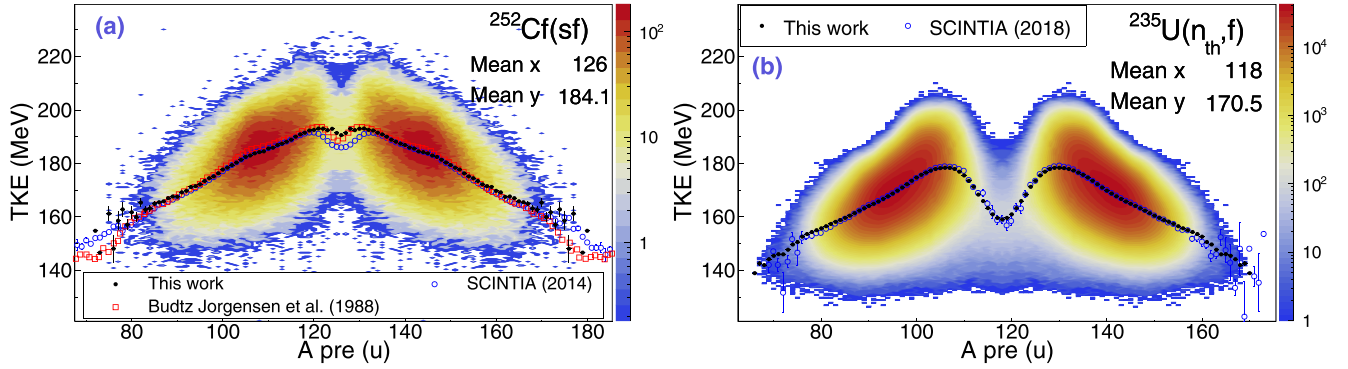


FIG. 18. (a) The TKE distributions versus preneutron emission mass for  $^{252}\text{Cf}(\text{sf})$ . (b) The same two-dimensional distribution for  $^{235}\text{U}(\text{n}_{\text{th}}, \text{f})$ . In both cases the  $\overline{\text{TKE}}(A)$  is plotted on top together with the literature data [5,10,11].

neutron-emission values (1.390/1.047 [22]). The discrepancies are large between our data and the Wahl systematics. In addition, the Wahl evaluation disagree with all four data sets for most heavy fragments. This indicates a clear need for a new prompt-fission neutron multiplicity evaluation. For the  $\overline{\nu}(\text{TKE})$  in  $^{235}\text{U}(\text{n}_{\text{th}}, \text{f})$ , the slope is  $\partial\overline{\text{TKE}}/\partial\overline{\nu} = (-12.0 \pm 0.1)$  MeV/n, which is in perfect agreement with the value at epithermal energy  $(-12.0 \pm 0.2)$  MeV/n [5]. The values of Refs. [6,7] are significantly lower (between  $-16.7$  and  $-18.5$  MeV/n). The discrepancy has been shown earlier to be caused by resolution effects [5], because a degraded energy resolution results in a violation of the  $Q$ -value limit and an erroneous increase in  $\partial\overline{\text{TKE}}/\partial\overline{\nu}$  in Refs. [6,7].

### C. Uncertainty estimation

The error bars plotted in the figures of this work only reflect the statistical uncertainties. The systematic uncertainties arise mainly from the neutron data cuts described in Sec. IV A and from the fragment-neutron analysis used to determine the yields, as discussed in Secs. III B and IV C.

The systematic uncertainties caused by the neutron-data treatment, including the effects of Eqs. (3) and (4), are mostly compensated by the normalization to the Mannhart evaluation, to a first approximation. The reported uncertainty of the evaluation, between 0.18 and 9.3 MeV is below 2% [27]. However, because the detection efficiency varies by maximum 30%, the contribution of this uncertainty to the neutron multiplicity, is

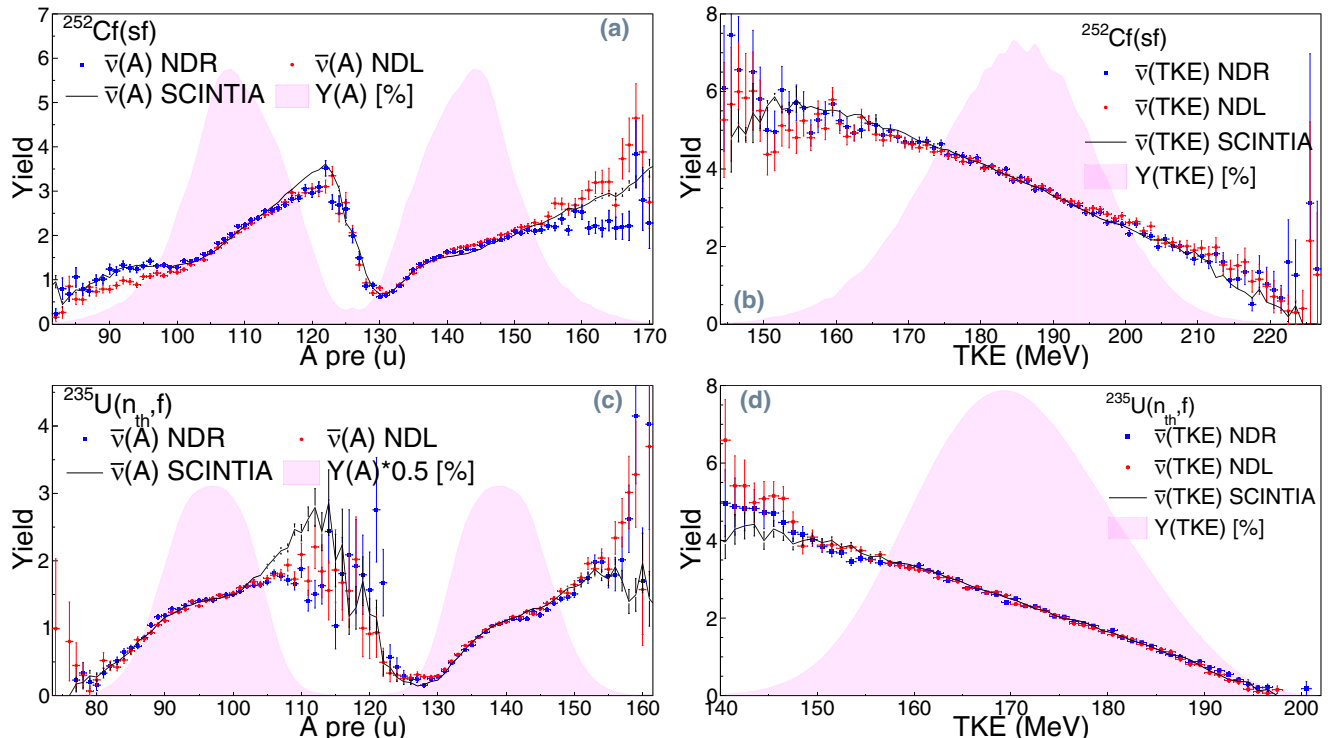


FIG. 19. The experimental prompt-fission neutron yield as a function of preneutron mass and TKE in  $^{252}\text{Cf}(\text{sf})$  and  $^{235}\text{U}(\text{n}_{\text{th}}, \text{f})$ . The data from both neutron detectors are displayed in comparison to SCINTIA results (full line) [5,11].

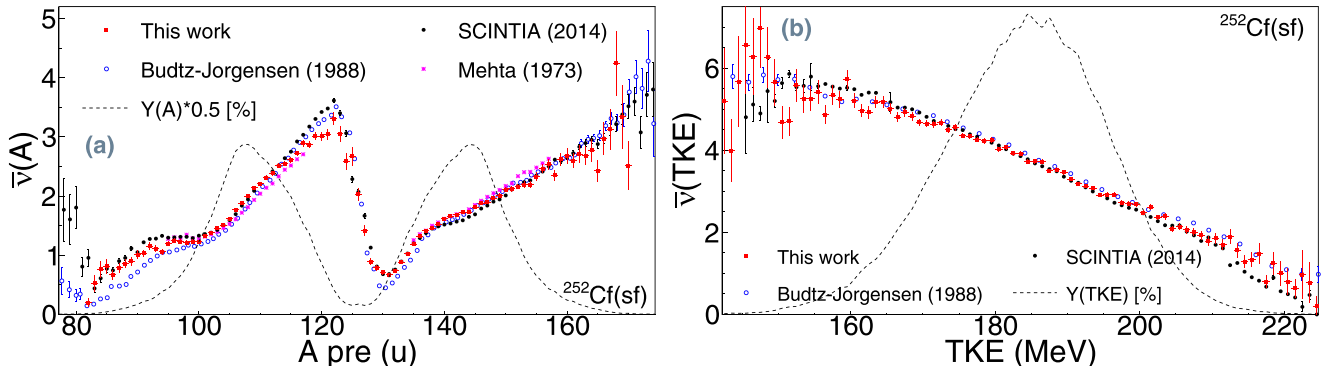


FIG. 20. (a) The  $\bar{\nu}(A)$  for  $^{252}\text{Cf}(sf)$  in comparison to literature data [10,11,43]. (b) The  $\bar{\nu}(TKE)$  for  $^{252}\text{Cf}(sf)$  in comparison to literature data [10,11].

below 0.6%, which is negligible compared to other sources of uncertainties.

The uncertainty due to the fragment-neutron analysis, including the angular selections and the impact of the mass resolution, was estimated from the simulated  $^{252}\text{Cf}(sf)$  data shown in Fig. 7. The errors are mass dependent since the  $\partial\bar{\nu}(A)/\partial A$  slope is altered. The systematic uncertainties for the  $\bar{\nu}(A)$  values in the peaks,  $A = 105$ – $116$ ,  $136$ – $153$ , is below 2%. For asymmetric masses,  $A < 105$  and  $A > 153$ , the uncertainties are up to 5%. At the maximum and minimum of the sawtooth curve, the error bars are at the highest and may reach 10–20%. It is worth noting that most literature neutron and fragment yield data suffer from similar uncertainties, caused by the unavoidable mass resolutions, even though it is often not reported.

#### D. Neutron energy as a function of fragment mass

The correlation between the neutron energy in the fragment rest frame ( $\eta$ ) and the fragment mass is shown in Fig. 22 for both reactions. The average energies as function of mass,  $\eta(A)$ , agree with the earlier data [10,11]. The trends in the average energy with respect to the symmetric mass  $A_{CN}/2$  are surprisingly symmetric, in contrast to the strong asymmetry in the sawtooth shape seen in Figs. 20 and 21 [42]. Some mass dependence is observed both in  $^{252}\text{Cf}(sf)$  and  $^{235}\text{U}(n_{th}, f)$ , with

varying average energies between 1 and 2 MeV and a higher energy in the symmetry region.

## VI. SUMMARY AND OUTLOOK

In this work we reported on two measurements performed at the EC-Joint Research Centre in Geel, Belgium. The goal was to measure the prompt-fission neutron multiplicities in  $^{235}\text{U}(n_{th}, f)$  and  $^{252}\text{Cf}(sf)$ . The experiment on  $^{235}\text{U}(n_{th}, f)$  was aimed as an extension of the recent epithermal neutron measurements at JRC. A secondary aim was to serve as a reference for an upcoming  $\bar{\nu}(A)$  measurement at higher excitation energies, to study energy sharing in the fission process. The recent epithermal data obtained with SCINTIA, showed surprisingly large deviations from earlier thermal fission neutron data. The differences could either be due to a different excitation energy or from advances in instrumentation, simulations, and refined data analysis. Our data confirm the epithermal data and that the discrepancies are not attributed to the excitation energy. It should be noted that, although we use similar techniques, an independent analysis was performed and different detectors, targets, and accelerator-based neutron source were employed. Moreover, a thermal neutron spectrum has been used in the present work, as opposed to the epithermal spectrum in case of SCINTIA.

Our experimental investigations employed a Twin Frisch-grid ionization chamber and two liquid scintillation detectors.

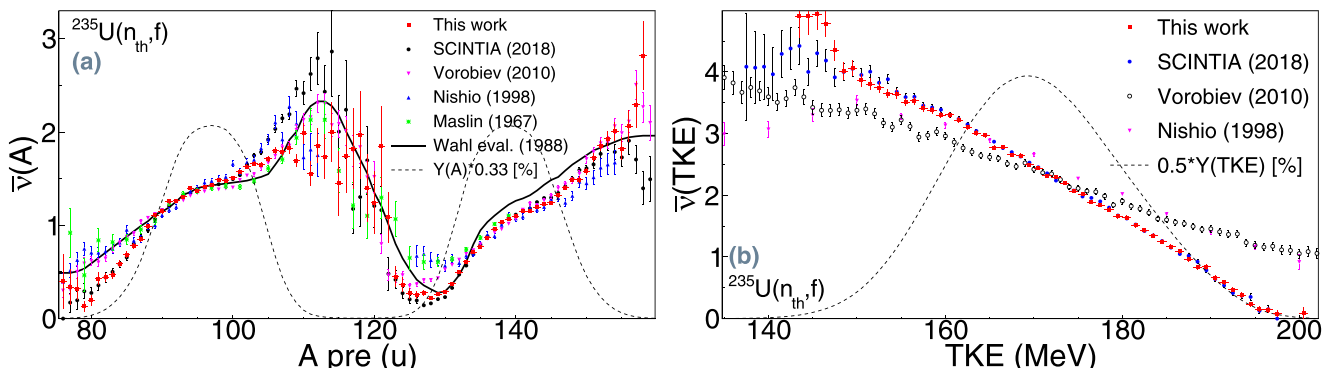


FIG. 21. (a) The  $\bar{\nu}(A)$  for  $^{235}\text{U}(n_{th}, f)$  in comparison to literature data [5–9]. (b) The  $\bar{\nu}(TKE)$  for  $^{235}\text{U}(n_{th}, f)$  in comparison to literature data [5–7].

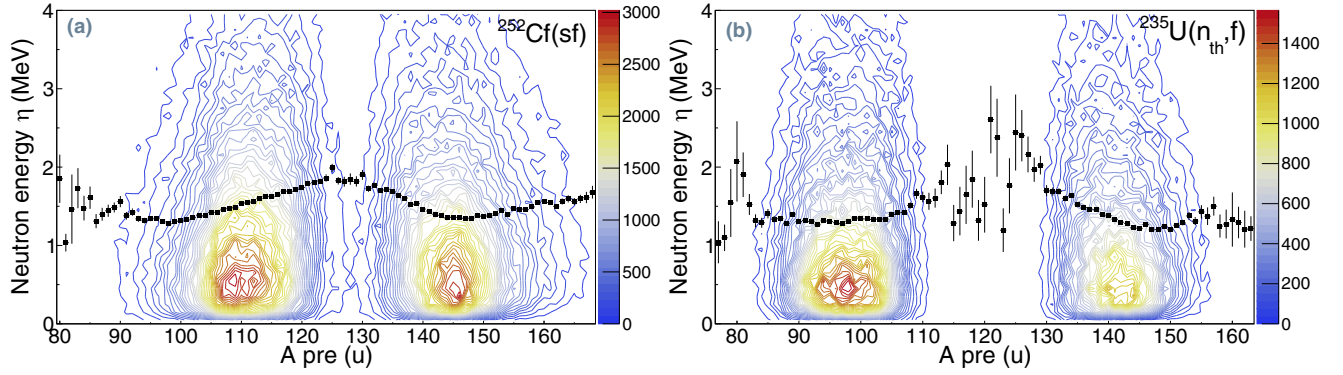


FIG. 22. The measured neutron spectrum in the fragment reference frame ( $\eta$ ) as a function of fragment mass, for  $^{252}\text{Cf}(sf)$  in (a) and for  $^{235}\text{U}(n_{th}, f)$  in (b). The mean energies are plotted as black circles.

The preneutron emission mass distributions were obtained via the two-energy method. The neutrons were produced via the 7 MV Van De Graaff accelerator and moderated with paraffin. FLUKA neutron simulations for the  $^{235}\text{U}(n, f)$  case showed that about 98% of all fission events were induced by thermal neutrons [0 eV, 0.26 eV]. The mass resolution was estimated to about  $\sigma_A = 2.3$  u in the case of  $^{235}\text{U}(n_{th}, f)$ . The  $\bar{\nu}(A)$  data were derived by a ratio of the coincidence and noncoincidence mass distributions.

In the first part of the work, we proved the validity of the technique, by performing detailed and comprehensive simulations, driven by the GEF code. The main conclusions of the simulation study were:

- (i) Despite the stringent kinematic cuts and necessary corrections, we confirmed the applied methodology and the validity of the extracted neutron multiplicities.
- (ii) The mass resolution affects the final  $\bar{\nu}(A)$ , most significantly causing a decrease in  $\partial\bar{\nu}(A)/\partial A$ . However, the main features of the  $\bar{\nu}(A)$  presented in our work remain nearly unaffected, considering the actual mass resolution ( $\sigma_A = 2.3$  u).
- (iii) The  $\bar{\nu}(\text{TKE})$  was found to be rather robust against resolution effects, at least considering smearing in the order of  $\sigma_E = 0.5$  MeV, in the single fragment energy. Poor energy resolutions affect the shape by introducing smaller  $\partial\bar{\text{TKE}}/\partial\bar{\nu}$  values and thus rendering nonphysical results.

In the second part, we presented the experimental results from the ionization chamber and the two neutron detectors. The chamber results were in good agreement with earlier data, both in terms of mass yields and total kinetic energy distributions. The measured neutron spectra (PFNS), in the center-of-mass system, were fitted with the neutron evaporation cascade model, resulting in the fit parameters:  $\lambda = (0.385 \pm 0.01)$ ,  $T_{\text{eff}} = (1.031 \pm 0.007)$  MeV for  $^{252}\text{Cf}(sf)$ , and  $\lambda = 0.5$ ,  $T_{\text{eff}} = (0.847 \pm 0.002)$  MeV for  $^{235}\text{U}(n_{th}, f)$ .

The presented prompt-fission neutron data are in excellent agreement with the epithermal data from SCINTIA and confirmed the observed discrepancy to the other literature data. For the  $^{252}\text{Cf}(sf)$  data, the average neutron emission values for light and heavy fragments were found to be  $\bar{\nu}_{\text{tot,L}} = 2.04$  and  $\bar{\nu}_{\text{tot,H}} = 1.72$ . For  $^{235}\text{U}(n_{th}, f)$  they were  $\bar{\nu}_{\text{tot,L}} = 1.41$  and  $\bar{\nu}_{\text{tot,H}} = 1.02$ . The  $\partial\bar{\text{TKE}}/\partial\bar{\nu}$  was found to be  $(-12.9 \pm 0.2)$  MeV/n for  $^{252}\text{Cf}(sf)$ , and  $(-12.0 \pm 0.1)$  MeV/n for  $^{235}\text{U}(n_{th}, f)$ .

In conclusion, the new results may help to better understand fission and fragment deexcitation. It may guide evaluators to improve the modeling of fission-neutron emission. The recent investigations by JRC-Geel and Uppsala University clearly confirm the lack of accurate correlation fission data even in the best-studied reactions, such as  $^{235}\text{U}(n_{th}, f)$ . And, we know that discrepancies between data sets grow at higher excitation energies. In the future we plan to measure the fast-neutron-induced fission of a few actinides, to investigate how  $\bar{\nu}(A)$  and  $\bar{\nu}(\text{TKE})$  change as a function of excitation energy. This will constrain fission models and help to fine tune them to describe nuclear deexcitation more accurately.

## ACKNOWLEDGMENTS

The authors would like to thank the Joint Research Centre, for supporting these experimental activities through the EUFRAT program. This work was also supported by the European Commission within the Seventh Framework Program through Fission-2013-CHANDA (Project No. 605203), the Swedish Radiation Safety Authority, SSM (project SSM2018-1587) and the Swedish Centre for Nuclear Technology (SKC). The MONNET team of the JRC-Geel is acknowledged for providing the neutron beam and for the technical support. The Target Preparation Group of JRC-Geel is acknowledged for the preparation of the high-quality uranium target. A.A. would like to acknowledge Harald och Louise Ekmans Forskningsstiftelse (Sigtunastiftelsen) and Ingegerd Berghs stiftelse, for their research grants.

[1] J. S. Fraser and J. C. D. Milton, Distribution of prompt-neutron emission probability for the fission fragments of  $\text{U}^{233}$ , *Phys. Rev.* **93**, 818 (1954).

[2] R. Vandenbosch, Dependence of fission fragment kinetic energies and neutron yields on nuclear structure, *Nucl. Phys.* **46**, 129 (1963).

- [3] M. Albertsson, B. Carlsson, T. Døssing, P. Möller, J. R. rup, and S. Åberg, Excitation energy partition in fission, *Phys. Lett. B* **803**, 135276 (2020).
- [4] A. Al-Adili, F.-J. Hamsch, S. Pomp, and S. Oberstedt, Sensitivity of measured fission yields on prompt-neutron corrections, *Nucl. Data Sheets* **119**, 342 (2014).
- [5] A. Gook and F.-J. Hamsch, and S. Oberstedt, and M. Vidali, Prompt neutrons in correlation with fission fragments from  $^{235}\text{U}(n, f)$ , *Phys. Rev. C* **98**, 044615 (2018).
- [6] K. Nishio, Y. Nakagome, H. Yamamoto, and I. Kimura, Multiplicity and energy of neutrons from  $^{235}\text{U}(n_{th}, f)$  fission fragments, *Nucl. Phys. A* **632**, 540 (1998).
- [7] A. Vorobyev, O. Shcherbakov, A. Gagarski, G. Valski, and G. Petrov, Investigation of the prompt neutron emission mechanism in low energy fission of  $^{235,233}\text{U}(n_{th}, f)$  and  $^{252}\text{Cf}(sf)$ , *EPJ Web Conf.* **8**, 03004 (2010).
- [8] A. C. Wahl, Nuclear-charge distribution and delayed-neutron yields for thermal-neutron-induced fission of  $^{235}\text{U}$ ,  $^{233}\text{U}$ , and  $^{239}\text{Pu}$  and for spontaneous fission of  $^{252}\text{Cf}$ , *At. Data Nucl. Data Tables* **39**, 1 (1988).
- [9] E. E. Maslin, A. L. Rodgers, and W. G. F. Core, Prompt neutron emission from  $\text{U}^{235}$  fission fragments, *Phys. Rev.* **164**, 1520 (1967).
- [10] C. Budtz-Jørgensen and H.-H. Knitter, Simultaneous investigation of fission fragments and neutrons in  $^{252}\text{Cf}(SF)$ , *Nucl. Phys. A* **490**, 307 (1988).
- [11] A. Gook, F.-J. Hamsch, and M. Vidali, Prompt neutron multiplicity in correlation with fragments from spontaneous fission of  $^{252}\text{Cf}$ , *Phys. Rev. C* **90**, 064611 (2014).
- [12] C. Budtz-Jørgensen, H.-H. Knitter, C. Straede, F.-J. Hamsch, and R. Vogt, A twin ionization chamber for fission fragment detection, *Nucl. Instrum. Meth. A* **258**, 209 (1987).
- [13] A. Al-Adili, F.-J. Hamsch, S. Oberstedt, S. Pomp, and S. Zeynalov, Comparison of digital and analog data acquisition systems for nuclear spectroscopy, *Nucl. Instrum. Methods Phys. Res. A* **624**, 684 (2010).
- [14] G. Battistoni, T. Boehlen, F. Cerutti, P. W. Chin, L. S. Esposito, A. Fassó, A. Ferrari, A. Lechner, A. Empl, A. Mairani, A. Merighetti, P. G. Ortega, J. Ranft, S. Roesler, P. R. Sala, V. Vlachoudis, and G. Smirnov, Overview of the FLUKA code, *Ann. Nucl. Energy (Oxford)* **82**, 10 (2015).
- [15] T. Böhlen, F. Cerutti, M. Chin, A. Fasó, A. Ferrari, P. Ortega, A. Mairani, P. Sala, G. Smirnov, and V. Vlachoudis, The FLUKA Code: Developments and challenges for high energy and medical applications, *Nucl. Data Sheets* **120**, 211 (2014).
- [16] V. Vlachoudis, FLAIR: A Powerful But User Friendly Graphical Interface For FLUKA, 2009.
- [17] N. Kornilov, I. Fabry, S. Oberstedt, and F.-J. Hamsch, Total characterization of neutron detectors with a  $^{252}\text{Cf}$  source and a new light output determination, *Nucl. Instrum. Meth. Phys. Res., Sect. A* **599**, 226 (2009).
- [18] E. Birgersson, and N. E. G. Lövestam, NeuSDesc-Neutron Source Description Software Manual, 2009.
- [19] K.-H. Schmidt, B. Jurado, C. Amouroux, and C. Schmitt, General description of fission observables: GEF model code, *Nucl. Data Sheets* **131**, 107 (2016).
- [20] K. Jansson, A. Al-Adili, E. A. Sundén, A. Göök, S. Oberstedt, and S. Pomp, The impact of neutron emission on correlated fission data from the 2E-2v method, *Eur. Phys. J. A* **54**, 114 (2018).
- [21] J. W. Boldeman, A. R. D. L. Musgrove, and R. L. Walsh, Prompt neutrons from  $^{236}\text{U}$  fission fragments, *Aust. J. Phys.* **24**, 821 (1971).
- [22] F. Gönnewein, *Neutron-induced fission* (La Villa Clythia, Fréjus France, 2014).
- [23] P.-A. Söderström, J. Nyberg, and R. Wolters, Digital pulse-shape discrimination of fast neutrons and  $\gamma$  rays, *Nucl. Instrum. Meth. Phys. Res. A* **594**, 79 (2008).
- [24] N. Kornilov, *Fission Neutrons - Experiments, Evaluation, Modeling and Open Problems* (Springer, Berlin, 2015).
- [25] H. W. Schmitt, J. H. Neiler, and F. J. Walter, Fragment energy correlation measurements for  $^{252}\text{Cf}$  spontaneous fission and  $^{235}\text{U}$  thermal-neutron fission, *Phys. Rev.* **141**, 1146 (1966).
- [26] A. Al-Adili, F.-J. Hamsch, S. Pomp, S. Oberstedt, and M. Vidali, Fragment-mass, kinetic energy, and angular distributions for  $^{234}\text{U}(n, f)$  at incident neutron energies from  $E_n = 0.2$  MeV to 5.0 MeV, *Phys. Rev. C* **93**, 034603 (2016).
- [27] W. Mannhart, Evaluation of the Cf-252 fission neutron spectrum between 0 MeV and 20 MeV, IAEA-TECDOC-410 18075519, 1987.
- [28] A. Al-Adili, F.-J. Hamsch, R. Bencardino, S. Pomp, S. Oberstedt, and S. Zeynalov, On the Frisch-Grid signal in ionization chambers, *Nucl. Instrum. Meth. Phys. Res. A* **671**, 103 (2012).
- [29] A. Gook, F.-J. Hamsch, A. Oberstedt, and S. Oberstedt, Application of the Shockley-Ramo theorem on the grid inefficiency of Frisch grid ionization chambers, *Nucl. Instrum. Meth. Phys. Res. A* **664**, 289 (2012).
- [30] A. Al-Adili, F.-J. Hamsch, R. Bencardino, S. Oberstedt, and S. Pomp, Ambiguities in the grid-inefficiency correction for frisch-grid ionization chambers, *Nucl. Instrum. Meth. Phys. Res. A* **673**, 116 (2012).
- [31] F.-J. Hamsch, J. van Aarle, and R. Vogt, Is there a pulse height defect for methane?, *Nucl. Instrum. Meth. Phys. Res. A* **361**, 257 (1995).
- [32] A. Al-Adili, Ph.D. thesis, Uppsala University, Sweden, 2013.
- [33] A. Al-Adili, F.-J. Hamsch, S. Pomp, and S. Oberstedt, Impact of prompt-neutron corrections on final fission-fragment distributions, *Phys. Rev. C* **86**, 054601 (2012).
- [34] F.-J. Hamsch and S. Oberstedt, Investigation of the far asymmetric region in  $^{252}\text{Cf}(sf)$ , *Nucl. Phys. A* **617**, 347 (1997).
- [35] H. Baba, T. Saito, N. Takahashi, A. Yokoyama, S. M. Takahiro Miyachi, D. Yano, T. Hakoda, K. Takamiya, K. Nakanishi, and Y. Nakagome, Role of effective distance in the fission mechanism study by the double-energy measurement for uranium isotopes, *J. Nucl. Sci. Technol.* **34**, 871 (1997).
- [36] P. Geltenbort, F. Gönnewein, A. Oed, and P. Perrin, Mass spectrometry of fission fragments by simultaneous energy and time-of-flight measurements, *Radiat. Eff.* **95**, 325 (1986).
- [37] E. Birgersson, A. Oberstedt, S. Oberstedt, and F.-J. Hamsch, Properties of the reaction  $^{238}\text{U}(n, f)$  at the vibrational resonances, *Nucl. Phys. A* **817**, 1 (2009).
- [38] K. L. Couteur and D. Lang, Neutron evaporation and level densities in excited nuclei, *Nucl. Phys.* **13**, 32 (1959).
- [39] V. Weisskopf, Statistics and nuclear reactions, *Phys. Rev.* **52**, 295 (1937).
- [40] A. Gavron, Correction of experimental results in fission experiments: Ii. neutron yield corrections, *Nucl. Instrum. Meth.* **115**, 99 (1974).



- [41] A. Al-Adili, K. Jansson, D. Tarrío, F.-J. Hamsch, A. Göök, S. Oberstedt, M. O. Frégeau, C. Gustavsson, M. Lantz, A. Mattera, A. V. Prokofiev, V. Rakopoulos, A. Solders, M. Vidali, M. Österlund, and S. Pomp, Studying fission neutrons with 2E-2v and 2E, *EPJ Web Conf.* **169**, 00002 (2018).
- [42] C. Wagemans, *The Nuclear Fission Process*, 1st ed. (CRC Press Inc, 1991).
- [43] G. K. Mehta, J. Poitou, M. Ribrag, and C. Signarbieux, Detailed study of alpha emission in  $^{252}\text{Cf}$  fission, *Phys. Rev. C* **7**, 373 (1973).